RF SHIELDING OPTIMIZATION FOR NON PLANAR SURFACES IN INTERVENTIONAL MRI

by

Çağla Özsoy

Bachelor of Science, in Mechatronics Engineering, Marmara University, 2014

Submitted to the Institute of Biomedical Engineering
in partial fulfillment of the requirements
for the degree of
Master of Science
in
Biomedical Engineering

Boğaziçi University
2017

RF SHIELDING OPTIMIZATION FOR NON PLANAR SURFACES IN INTERVENTIONAL MRI

APPROVED BY:

Assist. Prof. Dr. Özgür Kocatürk .....
(Thesis Advisor)

Assist. Prof. Dr. Baykal Sarıoğlu .....

Prof. Dr. Cengizhan Öztürk .....

DATE OF APPROVAL: June 2017

ACKNOWLEDGMENTS

I would like to express my sincere gratitude to my supervisor Asst. Prof. Özgür Kocatürk for his support, knowledge, motivation and his patience during my M.Sc. study and research. His guidance helped me throughout my research and writing of this thesis. I would like to acknowledge Prof. Dr. Levent Değertekin (Georgia Institute of Technology / School of Electrical and Computer Engineering) for his guidance and his PhD student Yusuf Samet Yaraş for his contributions and valuable comments on this thesis. I would like to thank Assoc. Prof. Arda Deniz Yalçınkaya for his insightful comments and his permission for using his laboratory. I would like to thank Assoc. Prof. Bora Garipcan (Boğaziçi University / Institute of Biomedical Engineering) and his PhD students Fatma Zehra Erko and Alp Özgün for their valuable contributions to this thesis. Also, I am grateful to Engin Baysoy and Ahmet Turan Talaş for enlightening me at the beginning of the research and for their help with the clean room studies.

I must express my very profound gratitude to my dear parents and my sister Başak for supporting me spiritually all the time. I would like to thank my friends from BETA Laboratory, and Micro Nano Measurement and Characterization Laboratory(MNL). I would also like to thank Naci Pekçokgüler for his help in many of my difficult moments. Finally, I would like to thank dear Kaan Oktay for his continuous encouragement and motivation whenever I felt stuck throughout the months of study and through the process of researching and writing this thesis.

This accomplishment would not have been possible without them. Thank you.

ACADEMIC ETHICS AND INTEGRITY STATEMENT

I, Çağla Özsoy, hereby certify that I am aware of the Academic Ethics and Integrity Policy issued by the Council of Higher Education (YÖK) and I fully acknowledge all the consequences due to its violation by plagiarism or any other way.

Name :

Signature:

Date:

ABSTRACT

RF SHIELDING OPTIMIZATION FOR NON PLANAR SURFACES IN INTERVENTIONAL MRI

Magnetic Resonance Imaging (MRI) is a potential candidate for interventional cardiovascular procedures since it is ionizing radiation-free and thus safe for human use. However current devices suffer from mechanical and electrical constraints and face with safety issues. Interventional MRI devices incorporate RF receiver antenna and long transmission lines for active visualization purpose are prone to RF induced heating. Therefore, alternative non-metallic transmission line technologies such as acousto-optic transmission line has been developed. The ultrasonic transducers used in acousto-optic transmission lines can couple with local E-field changes during MRI scan and generate noise. This work aims to develop RF shielding coating methodology on non-planar surface to achieve the highest sensitivity for signal transmission by eliminating , noise generating factors. For this purpose, a compact housing design was constructed for the piezoelectric transducer that is coupled with an optical transmission line and a radio frequency solenoid coil. Also, the cross-talk between the ultrasound transducer and Magnetic Resonance Imaging scanner's electric field aimed to be removed using different shielding materials. Shielding effectiveness simulations were performed by using $CST^{®}$ software and measurements were performed within a gelled phantom as described in the ASTM F2182 standard. RF performances of the antennas and different shielding materials were measured using a vector network analyzer in terms of the scattering parameters. Network analyzer results demonstrated that MRI compatible copper powder-epoxy combination and conductive silver ink are feasible RF shielding materials because they show similar behavior compare to pure copper material.

Keywords: Interventional Cardiovascular MRI, RF Shielding

ÖZET

GİRİŞİMSEL MANYETİK REZONANS GÖRÜNTÜLEMEDE DÜZLEMSEL OLMAYAN YÜZEYLER İÇİN RF KALKAN OPTİMİZASYONU

Manyetik Rezonans Görüntüleme (MRG), iyonize radyasyon içermemesi sebebiyle girişimsel kardiyo vasküler prosedürleri için potansiyel bir adaydır. Halihazırdaki aygıtların tasarımı mekanik ve elektriksel sınırlar ve emniyet gerekliliklerinden dolayı zorlu hale gelmiştir. Radyo Frekans (RF) alıcı anten ile uzun iletim hatları içeren ve aktif görüntüleme amacıyla kullanılan girişimsel MRG cihazları, RF kaynaklı ısınma eğilimindedirler. Bu nedenle, metalik iletim hattı içermeyen alternatif teknolojiler; örneğin, akusto-optik iletim hatları geliştirilmiştir. Akusto-optik iletim hatlarında kullanılan ultrasonik dönüştürücüler elektrik alanı değişikliklerinden etkilenerek gürültüye sebep olabilmektedirler. Bu çalışma, gürültüyü oluşturan faktörleri yok etmek ve yüksek hassasiyette sinyal iletimi sağlamak için, planar olmayan yüzeyler üzerinde bir RF kalkanı geliştirmeyi amaçlamaktadır. Bu amaçla, RF alici anten ve optik fiberle bütünleşik bir ultrasonik dönüştürücüyü içeren MRG uyumlu sinyal iletim hattı için tasarlanmış kompakt bir RF kalkanı tasarlanmış ve üretilmiştir. Aynı zamanda, elektromanyetik alan ile etkileşiminden koruma amacıyla farklı materyaller kullanılarak, ultrasonik dönüştürücü üzerinde MRG cihazının elektrik alanından dolayı oluşan gürültünün giderilmesi amaçlanmıştır. RF koruma etkinliği $CST^{®}$ programında test edilmiş ve ölçümler ASTM F2182 standardında belirtildiği şekilde hazırlanan jelleştirilmiş fantom içerisinde gerçekleştirilmiştir. Farklı materyaller ve hazırlanan antenlerin RF performansları vektör network analizör ile değerlendirilmiştir. Saf bakır materyali ile karşılaştırıldığında benzer davranışı göstermesi sebebiyle MRG uyumlu bakır tozu-epoksi karışımı ve iletken gümüşün, RF koruma için elverişli olduğu gösterilmiştir.

Anahtar Sözcükler: Girişimsel Kardiyovasküler MRG, RF Kalkan

TABLE OF CONTENTS

LIST OF FIGURES

LIST OF TABLES

LIST OF SYMBOLS

Fr	French, catheter scale
mA	Milliamperes, electric current unit
Gd	Gadolinium
NaCl	Sodium Chloride

LIST OF ABBREVIATIONS

RF	Radio Frequency
MRI	Magnetic Resonance Imaging
iCMRI	Interventional Cardiovascular Magnetic Resonance Imaging
SAR	Specific Absorption Ratio
IEC	International Electrotechnical Commission
FDA	US Food and Drug Administration
FSP	Ferromagnetic Signal Pattern
Fe-Cath	Ferromagnetic catheters
Rad-Cath	Radiographic catheters
SPION	Superparamagnetic Iron Oxide Nanoparticles
FLAP	Fast Low-Angle Positive Contrast Steady-State Precession
FOV	Field of View
SSFP	Steady-State Free Precession
NMR	Nuclear Magnetic Resonance
TrueFISP	True Fast Imaging with Steady Precession
SNR	Signal-to-Noise Ratio
EO	Electro-optic
Gd-DTPA	diethylenetriamine penta-acetic acid
OFS	Optical Fiber Sensors
FBG	Fiber Bragg Grating
PZT	Lead-Zirconate-Titanate
ASTM	American Society for Testing and Materials
EM	Electromagnetic
PAA	Polyacrylic Acid
LDPE	Low Density Polyethylene
SE	Shielding Effectiveness

1. INTRODUCTION

Conventional fluoroscopy guidance for interventional procedures require a safe and effective alternative due to the lack of adequate soft tissue contrast and potential risk in cancer development following the procedure. According to Scientific Committee on Emerging and Newly Identified Health Risks (SCENIHR) "Potential health effects of exposure to electromagnetic fields (EMF)" report (27 Jan 2015), there is no direct evidence that human exposure to electromagnetic fields (EMF) cause brain tumour or cancer. With this in mind Magnetic Resonance Imaging (MRI) offers a safe and convenient alternative to X-ray fluoroscopy with its real-time and multiplanar imaging capabilities.

MRI is a promising solution for Interventional Cardiovascular Magnetic Resonance Imaging (iCMRI) procedures when compared to conventional imaging modalities. Currently, MRI compatible interventional devices are still under development since manufacturing conspicuous, mechanically and electrically convenient devices is challenging task to meet all the requirements. Also it is a challengng engineering task to satisfy MR safety requirements while conforming physical dimensions. Interventional procedures used in diagnosis and treatment of the congenital heart diseases (i.e. ventricular septal defect and atrial septal defect) instead of open surgery [10]. Those interventions are being made under fluoroscopy, thus have numerous potential hazards especially to pediatric patients [11]. Interventional procedures under MRI have been implemented in many different endovascular diseases including the renal artery stenosis treatment [12], abdominal aortic aneurysms treatment [13], recanalization of carotid chronic total occlusion [10], atrial septal puncture [14] and transcatheter aortic valve implantation [15] and electrophysiology mapping for atrial fibrillation treatment [16], [17] and [18]. Active visualization of interventional devices under MRI is quite appealing for clinicians during real time device tracking under MRI. However, long conductive transmission lines used in active devices causes RF induced heating. Recently, acousto-optic transmission line concept has been introduced that replaces the long transmission

lines with fiber optic cables [97]. The acousto-optic detection method is shown to be very robust and is widely used for measuring ultrasound fields for therapeutic and medical imaging applications and nondestructive testing through ultrasound induced strain measurements.

In this concept, active devices incorporates a distal loop antenna that is electrically connected to an ultrasonic transducer having a comparable profile. The ultrasonic transducer converts the electrical input from the coil to elastic waves at one end of an optical fiber with an embedded interferometric detection structure i.e. Fiber Bragg grating (FBG). The elastic waves over the grating result in acousto-optical modulation of the grating which is detected by a laser coupled to the proximal end of the optical fiber that runs along the active catheter shaft and transform to RF signal through a photo diode.

The purpose of this thesis is to optimize RF shielding coating on non-planar surfaces so that we can design RF shielding housing on the ultrasonic transducer of an acousto-optic transmission line to enhance the spatial resolution of the receiver antenna signal on interventional devices. To develop an active guiding catheter incorporating acousto-optic transmission line and RF receiver loop antenna, we closely collaborated with Professor Dr. Levent Degertekin at Georgia Tech. Dr. Degertekin's group designed and implemented the acousto-optical sensor and our receiver coil coupled with the ultrasound transducer on FBG embedded optical fiber.

1.1 List of publications produced from the thesis

1. Acousto-optic Based Active MRI Marker for Interventional MRI Devices, Y. S. Yaras, S Satir, C Ozsoy, R Ramasawmy, A E Campbell-Washburn, A Faranesh, R Lederman, O Kocaturk, L Degertekin, " *25th Annual Meeting and Exhibition International Society for Magnetic Resonance Imaging in Medicine (ISMRM 2017),Honolulu, HI, USA*, Apr. 22–Apr. 27, 2017.

2. BACKGROUND

Recently there has been an inclination towards interventional catheterization procedures under MRI guidance since Magnetic Resonance Imaging provides superior soft tissue visualization, real-time image acquisition and non-ionized radiation. However, currently there is no completely Magnetic Resonance (MR) compatible device for the catheter-based interventional cardiovascular procedures. In particular, interventional MRI had been used for treatment of cardiovascular diseases i.e. atrial or ventricular septal defects, cardiac rhythm disorders and coarctation of cardiac vessels [19]. However, because of the continuous motion of aorta, interventional procedures are complicated rather than the peripheral vessels [20]. Electric and magnetic dipole moments composed depending on the particle's inherent characteristics i.e. mass, mobility, due to electric and magnetic fields, and subsequent composed kinetic energy is distributed with the particle collisions which is the basis of the macroscopic level "radiofrequency heating effect".

According to ASTM International F2503 guidelines, medical devices used during MR scanning should be labeled as "MR safe", "MR unsafe", or "MR conditional" [21], [22]. A medical device is called MR safe if it is unconditionally safe in the MR environment and MR conditional if it is safe under certain criteria i.e. main magnetic field strength, maximum magnetic field gradient, maximum Specific Absorption Rate(SAR). SAR unit is energy per unit mass in tissue and SAR limit generally defined as stored energy in tissue should not cause temperature rise higher than 1^oC [22].

2.1 Conventional Procedures

Magnetic Resonance Imaging modality offers a safe, ionized free, functional, multiplanar and real time imaging [23], while conventional procedures suffer from soft tissue visualization and ionized radiation. Ionization takes place when a charged particle has adequate energy (higher than the orbital binding energy) to eject an electron

from its orbital [24]. Photons like x-rays and gamma-rays are capable of remove a bound electron and thus cause ionization however lower energy levels such as microwave and radio wave levels do not cause ionization. The amount of energy absorbed by matter (tissue), described by Linear Energy Transfer, which is approximately $3keV/\mu m$ for soft tissue during x-ray exposure. Effects of X-Ray radiation in the sub-atomic level can be explained with Rayleigh scattering, Photoelectric absorption, and Compton scattering. In Rayleigh scattering, incident photons are scattered in a different direction. In the photoelectric effect, incident photon with adequate energy (i.e. required for ionization), breaks an electron from the outer shell and the free electron's energy equals to the difference between incident photon and electron work function (energy difference between vacuum level and fermi level) energies. In the Compton effect, incident photon causes electron ejection and because of the energy loss, wavelength of the scattered quantum is longer than the incident quantum. While utilizing a medical imaging modality, radiation biology is a matter of vital importance. What determines the magnitude of the damage depends on several parameters such as radiation type and rate and biological matter as well. Radiation has stochastic effects which are not related with the amount of dose, there is one consequence which may occur such as cancer development and it has deterministic effects which occurs related with the amount of exposed radiation such as skin damages. Dangerous consequences by the interaction of radiation with tissue explained by Bushberg et.al. [24]. According to National Council on Radiation Protection and Measurements (NCRP,2009) report, regarding the medical radiation dose exposure, Computer Tomography (CT) and Nuclear Medicine have become the leading sources. Conventional and Interventional radiography/fluoroscopy have become the following sources in recent years [25]. Especially pediatric patients with congenital heart diseases are exposed to ionizing radiation thus they are more susceptible to cancer development in the following years [11]. Radiation dose and number of interventions whether for diagnosis or treatment, increases the severity of carcinogenic effects.

2.2 Interventional Cardiovascular Magnetic Resonance Imaging

Interventional procedures are being used in cardiovascular disease diagnosis is of vital importance especially for congenital heart disease diagnosis and treatment as well [26]. Catheterization is a technique used to reach the cardiovascular system via blood vessels (vein and arteries). iCMRI devices are categorized as passive, active, semi-active and also there are optical designs. MRI based catheterization is a ionized radiation free and conspicuous alternative. However, none of these techniques compromise all conditions (i.e. kink resistance, pushability, visibility, trackability, safety) in the same design [27], [26], [28] and [29].

2.2.1 MR-Safety Concerns and RF Heating

Magnetic Resonance Imaging principle is based on alignment of magnetic dipoles of atoms (magnetomechanical interaction). Therefore, especially when exposed to strong static field, metallic parts, i.e. implantable devices, pacemakers, defibrillators etc., should be avoided inside the MR room due to ferromagnetic materials acceleration under static magnetic field [30].

Human body due to its nature tend to maintain its temperature with thermoregulatory system despite environmental factors [31]. Specific Absorption Ratio spatially specifies the amount of the RF exposure absorbed by the human body during the MRI procedure. It is related with the electric field and the conductivity of the tissue and expressed as in 2.1 [32]:

$$SAR = -\frac{\sigma E^2}{2\rho_t} \tag{2.1}$$

where E is the Electric field, rho is the mass density and sigma is the conductivity

of the tissue. Interventional MRI devices have been investigated in terms of potential heating around metallic devices [33]. Especially long metallic components have the potential for heating during MRI RF excitation [34, 35, 36, 37, 38] In order to eliminate the RF heating problem several methods have been developed, i.e. RF chokes [39] or adding transformers to the transmission line [40], detuning the device during the RF transmission [41] and modifying the transmit coil to manipulate the electric field distribution around and implant during RF pulse transmission [42] as well.

Previous implementations increase safety of interventional devices by aiming to eliminate RF heating causes; however, they suffer from mechanical constraints and elevated average SAR values. Also, an informative transfer function model to predict the RF heating of metallic wires within the MRI phantom was developed by Atalar et. al. demonstrated in 2.1 [32], in which tissue specific dissipation "Bioheat Transfer" and metallic wire related power dissipation "SAR Gain" combined as the "Safety Index".

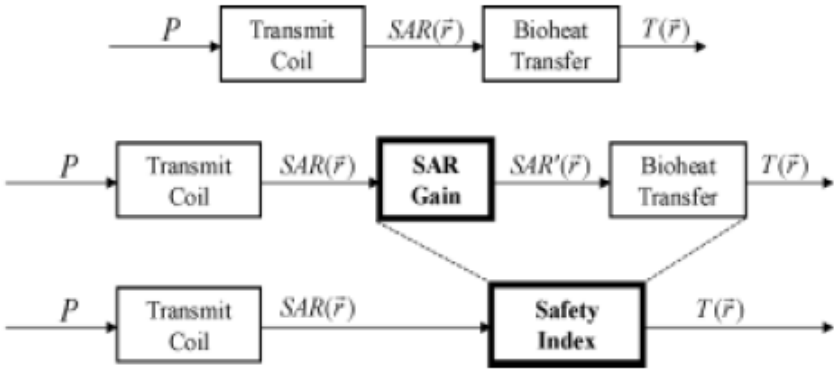

Figure 2.1 Model of RF heating in MRI [32].

Power loss occurring from the radiofrequency (RF) field in the metallic components and surrounding tissue distinguishes itself in heat energy. There are several causes for this occurrence, i.e. radiofrequency (RF) field composing eddy currents and currents composing due to the complex impedance difference between the tissue and the metal. Heating mainly occurs due to the dipole antenna behavior of conducting materials within the MR bore and the schematic can be seen in Figure(2.2) [43]. Electric field generated by the radiofrequency field in MRI, can be expressed as,

$$\overrightarrow{E_1} = \frac{1}{2}\omega\overrightarrow{r} \times \overrightarrow{B_1} \tag{2.2}$$

and induced voltage, current and maximum current i.e. spatially related derived in [43] accordingly,

$$V = \int_0^l E_1 \cdot dl, \tag{2.3}$$

$$i = \frac{V}{Z} \tag{2.4}$$

$$i(z) = i_0 \cos\frac{2\pi z}{\lambda} \tag{2.5}$$

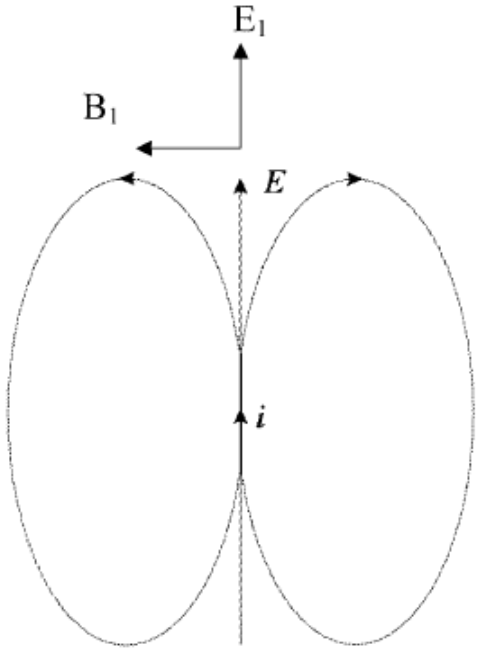

Figure 2.2 Dipole antenna behavior notation of the conductive wire [43].

Tissue surrounding the metallic wire heats due to the conduction current generated by the electric field expressed as $\overrightarrow{J} = \sigma\overrightarrow{E}$.

Finally, electrical power loss of the conductive wire and surrounding tissue can be calculated as in 2.6 and in 2.7 respectively.

$$P_{wire} = \frac{1}{2} {i_0}^2 R_{wire} \tag{2.6}$$

$$P_{wire} = \frac{1}{2} \int \overrightarrow{J} \cdot \overrightarrow{E} d^3 r, \tag{2.7}$$

Table 2.1 provides a guideline for RF Exposure on Specific Absorption Rate (SAR) and heating in human MRI studies prepared by International Electrotechnical Commission (IEC) and US Food and Drug Administration (FDA) [44].

Table 2.1
International Electrotechnical Commission (IEC) and US Food and Drug Administration (FDA) guidelines for RF Exposure on Specific Absorption Rate (SAR) and heating in human MRI studies [44].

Limit	Whole-Body Average	Heat Average	Head,Trunk Local SAR	Extremities Local
IEC (6-minute average) Normal (all patients)	$2W/kg(0.5^oC)$	$3.2W/kg$	$10W/kg$	$20W/kg$
IEC (6-minute average) First level (supervised)	$4W/kg(1^oC)$	$3.2W/kg$	$10W/kg$	$20W/kg$
IEC (6-minute average) Second level (IRB approval)	$4W/kg(> 1^oC)$	$> 3.2W/kg$	$> 10W/kg$	$> 20W/kg$
IEC (6-minute average) Localized heating limit	39^oC in 10g	38^oC in 10g		40^oC in 10g
FDA	$4W/kg$ for 15min	$3W/kg$ for 10min	$8W/kg$ in 1g for 10min	$12W/kg$ in 1g for 5min

2.3 Current Solutions and Limitations

2.3.1 Passive Devices

Passive devices offer a safe and feasible solution since they do not have electrical connections but on the other hand they provide poor precision regarding the device orientation [45]. There are several passive devices aiming visualization and tracking during the interventional procedures. Due to their magnetic susceptibility effect under MRI, ferromagnetic agent used catheters compared with conventional radiography catheters regarding the ferromagnetic agent concentrations and the orientation depending on the main magnetic field shown in Figure 2.3. Iron doped catheters (Fe-caths) produce Ferromagnetic Signal Patterns (FSPs) when it is perpendicular to the main magnetic field, on the other hand produce signal voids when it is parallel to the main magnetic field. Orientation changes the size of the FSPs. However Radiology Catheters (Rad-Caths) produce signal voids on both orientation and the origin of the signal voids is not possible to discriminate form other possible sources i.e. blood flow and air. Regardless their visibility when they are perpendicularly positioned to the main magnetic field; since the homogeneous dipole field (when placed paralled to the main magnetic field) cause no image distortion, and also create large artifacts at certain orientations [46], this limitations makes ferromagnetic materials inadequate [47].

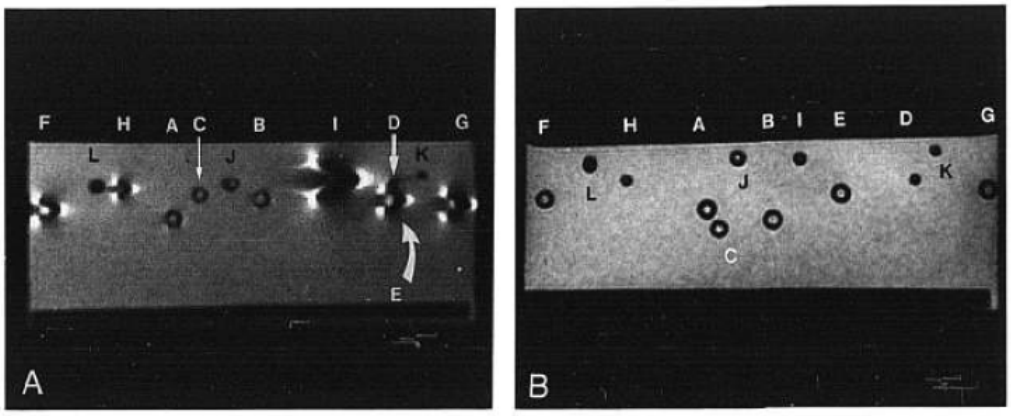

Figure 2.3 Signal void comparison between Fe-Caths (white letters) and Rad-Caths (black letters) imaged in a water bath; (A) Catheters oriented perpendicularly to the main magnetic field (B) Catheters oriented parallel to the main magnetic field [47].

Another study used superparamagnetic iron oxide nanoparticles (SPIONs) placed magnetic beads that increase the surrounding environment $T2^*$ relaxation time and thus enhance the image contrast in order to enhance the signal loss due to the strong background water signal. Microcoils used in order to detect the SPION placed magnetic beads in this study [48]. Low flip angles with the use of steady-state free precession method, off-resonant spins produce higher signal more than on-resonant spins and create positive contrast around the catheter and thus enhance the visibility of the devices discriminated susceptibility-shifted background. Precise localization and tracking of the interventional devices during in a procedure is a must. Regardless the effectiveness of the FLAPS visualization technique, because of the slice thickness limitation it is not possible to dynamically track the device [49]. Also, another interventional device passive imaging approach (project-reconstruction imaging with echo-dephasing) was implemented with the use of paramagnetic markers. Despite the method providing time efficiency, position accuracy remains a controversial issue [50].

Another paramagnetic compounds implemented catheters create local artifacts however the main problem is that this method requires additional image processing steps for especially dynamic regions [46]. Although Gadolinium (Gd) induced off-resonance contrast images created due to the bulk magnetization susceptibility frequency shifts of intravascular spins depending on the orientation to the main magnetic field and background water and fat suppression, frequency shifts are highly dependent on the orientation this method is not repeatable [51]. Iron particles at the tip of the polymer based guidewires provide a passive device tracking technique due to the susceptibility artifact during low flip angle SSFP scans. Although the device position can be seen, the accuracy especially at high Field of View (FOV) required regions is not sufficient. Also, since the iron particles spread over some distance, false positive contrasts occurred [52]. Another passive visualization approach uses 19F nuclear magnetic resonance (NMR) suffers from FOV limitation and clinically uncertain chemical substance usage [53]. The last but not least passive device imaging method used CO_2 filled balloon catheters shown in Figure 2.4 with imaging enhanced SSFP sequence again obstructs tracking because of the low image resolution during catheter movement [54].

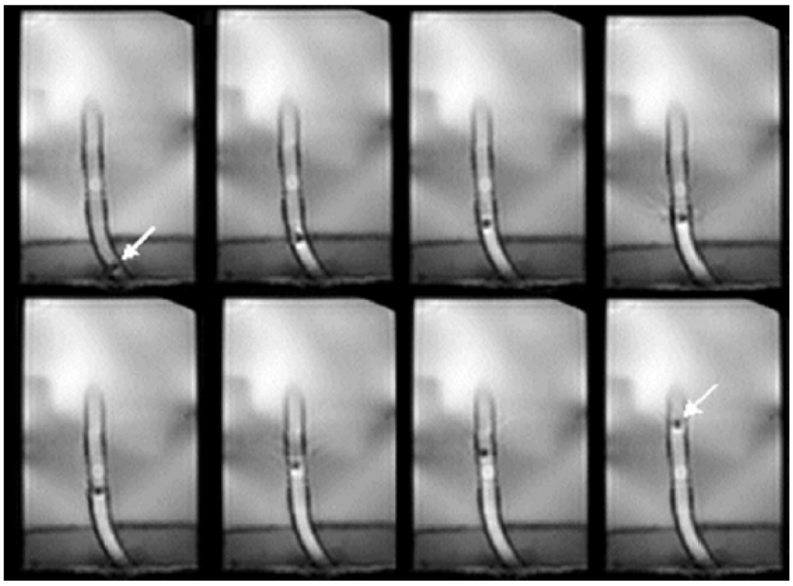

Figure 2.4 Images showing the catheter (arrow) being manipulated in the flow phantom [54].

2.3.2 Semi-Active Devices

Semi-active devices have become promising since they do not require an additional connection to the scanner through an electrical or an optical cable. Hybrid designs demonstrated that catheter visualization can be achieved using local field inhomogeneities. In this study, milliampere level currents applied to different solenoid coil configurations i.e. anti-parallel, twisted and separately wrapped wires made by copper in order to actively control the local magnetic inhomogeneity. Twisted pair wire arrangement and the first double helix concept into the interventional devices aiming to reduce radio frequency (RF) induced currents was introduced nevertheless safety concerns remained an issue. Figure 2.5 shows the inhomogeneity effects which result in clear visibility of the catheter, even in positions where it is close to the vessel wall [55].

Generally, excitation of one coil implemented configurations are highly dependent on the B1 field coupled with RC resonant circuits wounded on the endovascular catheters. In order to overcome the orientation dependency, they used perpendicularly decoupled two coils and thus at any orientation catheter tip became visible. However

Figure 2.5 Artifact of the introducer sheath in the right iliac artery in a pig study in which 5 Fr double helix catheter is used. (a) No current is applied. (b) 150 mA current is applied [55].

it is clear that active continuous tracking of those catheters was not achieved [56].

Thin copper wire winding around the catheter induce local inhomogeneities when a current applied. Due to the spin dephasing fast signal loss and thus black spots framed the catheter. The main problems were related with especially smaller anatomical regions, image artifacts created by the catheter obscured the anatomy itself and safety issues due to the energy deposition [57].

In another study, inductively coupled wireless loop coil configurations i.e. single-loop, Gianturco, helix, and solenoid and an external tuning capacitor used in order to achieve coupling with the main loop surface coil that acts as an RF receiver independently of the orientation. Desired quality factors obtained by its dependence on the transmitter and stent coil magnetic fluxes. Importance of this study is that it showed the significant decrease in the quality factor is primarily due to loading losses and lower flip angle excitations showed a better visualization. Since the shape of the coil alters during the procedure, resonant frequency was instable, reduced coupling between coils due to increased distance and also orientation dependency remained an issue [58].

Other studies show wireless inductively coupled catheter design which incorporates a single loop coil coupled to the surface coil during RF receive mode based on the orientation and increases the flip angle during RF transmit mode. The main

superiority of this design was that it provided higher flexibility regarding the catheter orientation to the main magnetic field as shown in Figure 2.6. Since active or passive decoupling mechanisms did not implemented, radio frequency heating due to magnetic field remained a significant concern [1].

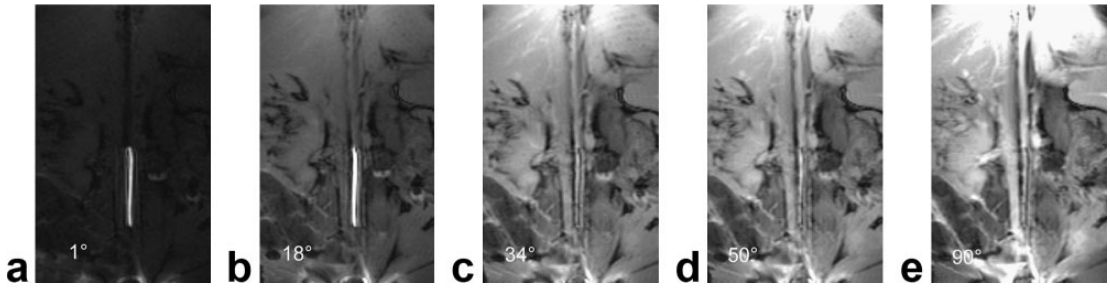

Figure 2.6 Variation of excitation flip angle and resulting changes in instrument to background signal in vivo. (a) Flip Angle=1^o. (b) Flip Angle=18^o. (c) Flip Angle=34^o. (d) Flip Angle=50^o. (e) Flip Angle=98^o [1].

In order to eliminate electronic components which require external power source for particularly safety reasons, an optical laser for detuning proposed. Based on the photoresistor working principle, in which resistance decrease with light thus decreasing the quality factor, current inducing on the coils became adjustable. Nevertheless, the photoresistor size was inapplicable for the clinical procedures [59].

Aiming to increase inductively-coupled radio frequency coil visualization sensitivity and not losing flip angle amplification during the RF transmission period with detuning methods, this method separately obtains catheter and background signals by means of reversely polarized birdcage coil. The theory primarily based on the discrimination between forward polarization of the excited spins and the linear polarization of the loop coils. Catheter tracking achieved by using inductively-coupled radio frequency coils and receive-coupled RF coils reduce heating significantly [60].

Recently, semi-active RF resonant marker has been developed by using novel microfabrication techniques to visualize catheter tip under MRI as in Figure 2.7. Since the design does not incorporate long transmission line and bulky electrical components unlike active devices, it is completely MRI safe and has a comparable profile [2].

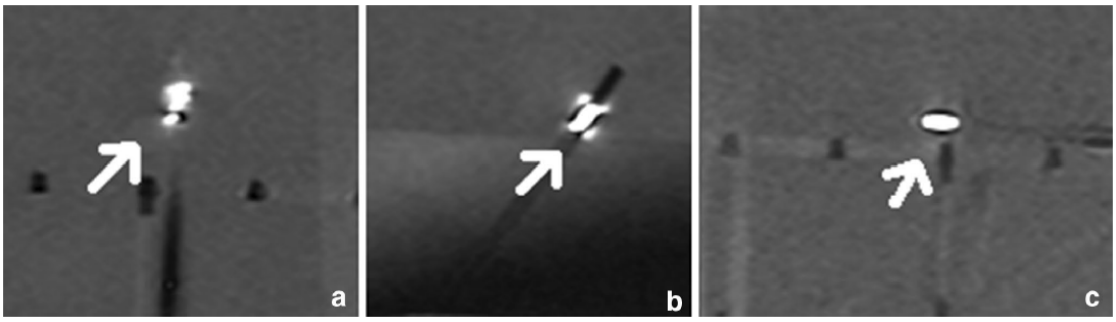

Figure 2.7 The RF resonant marker appeared as a bright spot under MRI 1.5 T. RF resonant marker when placed (a) parallel to the main magnetic field B0, (b) oriented 45^o relative to B0, and (c) placed perpendicular to B0 [2].

2.3.3 Active Devices

Active devices incorporate microcoils or RF antennas connected to the MR channel [61, 62, 63]. Major superiority of active devices is that they provide three dimensional temporal and spatial information thus increase the procedure success.

2.3.3.1 Microcoils. Tracking of active devices achieved by the further method. After a nonselective RF excitation, gradient in one direction applied. Since a microcoil is only capable to sense the very proximate MR signals, frequency peak received from the coil provides the location information [61]. Change in the magnetic field relatively effects the resonance frequency depending on the position. The underlying reason for using microcoils is that acquiring position dependent peak frequencies. Therefore, in order to have the three dimensional location information, one would need to apply gradients in both three directions. In order to overcome magnetic field distortions occuring due to magnetic susceptibility differences and thus resonance frequency errors, several methods have been applied. Oppositely polarized gradients with more than one excitation (Hadamard Encoding) applied in order to cancel the offset errors [63] and phase encoding gradient with frequency encoding gradient (phase field field dithering) applied in order to prevent more than desired MR signal occured due to microcoil and body coil coupling [62].

2.3.3.2 RF Antennas. One of the main antenna types including active devices are loop antennas (magnetically coupled). Ladd et.al. developed several antenna geometries as transmit and receive coils i.e. single loop, center return, crossed loop, solenoid, and their related magnetic field B1 has been calculated according to the Biot-Savart law which are demonstrated in 2.8 and 2.9. Regardless of the coil geometry, signal intensity increased due to the short T1 source within the coil. RF heating due to magnetic coupling remained problematic and unclear [64].

$$\vec{B_1} = -\frac{\mu_0}{4\pi} \oint \frac{I\vec{dl}x\hat{r}}{r^2} \tag{2.8}$$

$$S \propto \frac{B_1}{I} \cdot \frac{\partial M_0}{\partial t} dV = \frac{B_{1xy}}{I} M_0 dV \tag{2.9}$$

Radiofrequency solenoid coil placed at the tip of a guidewire used as an antenna as solenoid coils resulted a promising signal intensity in the previous study. The main outcome of this study is that design became orientation independent to the main magnetic field [4].

An active profiling needle developed as in Figure 2.8 in order to track the overall length under MRI by incorporating a loop antenna in the design. Despite the detuning precaution, because of the metallic components high current density and hence heating related safety concerns continued [3].

Figure 2.8 Active needle with close-up of tip uncovered (top) and covered (bottom) [3].

Twisted loop coils used in transmit and receive modes in order to visualize the overall device length [65].

Helical loop coil was implemented on a vascular guidewire reduce the orientation dependency to the main magnetic field. Loop coil and the body coil images were overlaid as shown in Figure 2.9. In this study, high contrast images achieved and entire length of the device could be visualized. The main drawback of the method is that the significant RF induced temperature increase during body coil transmit [4].

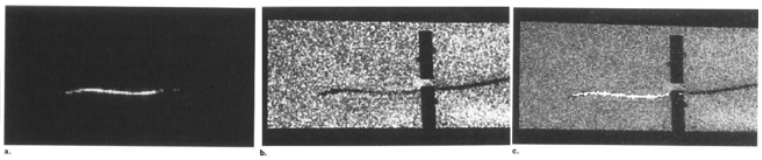

Figure 2.9 (a) Image acquired with guidewire coil. (b) Image acquired with body coil. (c) Overlay showing excellent position agreement [4].

RF receive coil implemented catheter connected to the fully shielded coaxial cable showed highest tracking signal peak after Fourier Transform when compared with the partially shielded and with the twisted pair cable. Although active real-time tracking achieved in this study, tip tracking instead of overall length remained unsolved [66].

In order to provide whole shaft visibility with dipole antennas and fulfil their low tip visibility with loop coils, both are connected in a one design. While solenoid coils create bright spots at the tip, dipole antenna provides continuous shaft visibility as in Figure 2.10. Besides its precise visualization, potential heating over long conductor lines due to electric field, prevented by detuning with the use of PIN diodes [5].

Second type of active devices include loopless antennas (electrically coupled). Thin active devices suffer from physical dimensional limitations due to the fact that acquired signal from smaller devices decrease as the diameter of the coil decreases and also signal from the coaxial cable becomes prominent and thus more than one peak frequencies occur. In this study rod antennas were analyzed in both parallel and perpendicular to the main magnetic field. [67].

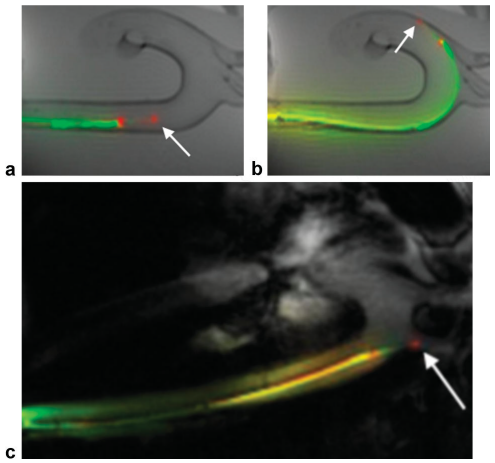

Figure 2.10 Representative MRI. (a) The long solenoid coil creates bright dots (red) at each end; the shaft is reconstructed on a separate channel (green). (b) Transfemoral guidewire in phantom aortic arch. Tip (arrow) deflection does not alter signal. (c) Transfemoral guidewire in vivo in brachiocephalic artery. Crosstalk is evident with surrounding tissue [5].

Previously since small SNR values provided by short circuited two conductors, tuning and matching circuits can not be placed far from the vessel in order to not to increase the noise signal [68] . In this study, in order to reduce the diameter without adhering to the electromagnetic restrictions, antenna was formed as a wire and thus higher signal and noise values acquired. In the Figure(2.11), the inner conductor and the secondary shield act as a dipole antenna while the dielectric material balances the current and thus no net current flows outside of the primary shield since the unbalanced currents effect the input impedance. Antenna resonates during the RF excitation and RF induced heating occurs, thus in order to prevent this effect by providing high input impedance with a pin diode during the RF excitation. An important outcome of this study was the acquisition of high SNR around the antenna by the signal sensitivity decrease as the radial distance increase [69].

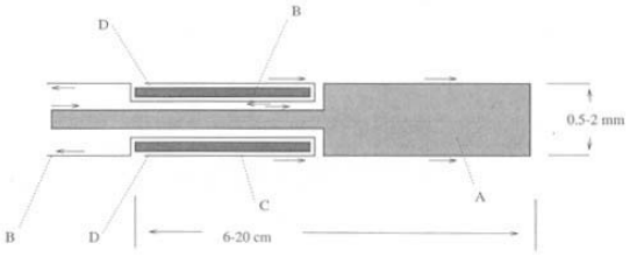

Figure 2.11 Sectional view of the catheter antenna. A, inner conductor; B, primary shield; C, secondary shield; D, high ϵ_r insulator.

In order to overcome the narrow and complex structure of the coronary arteries and motion related image artifacts, together with the surface coils, Nitinol guidewires including loopless antennas aimed to be used during coronary catheterization procedures with real-time Magnetic Resonance Imaging (MRI) guidance. Loopless antenna containing guidewire and guiding catheter were distinguished from the surrounding and were simultaneously visualized using two receiver channels [70].

In this study, although the active device was similar to the previous designs by incorporating dipole antennas and helical winding at the tip, in order to create simultaneously accurate images for device tracking purposes, previously maintained anatomical roadmap acquisition method replaced with true fast imaging with steady precession (TrueFISP) high frame rate imaging sequence which can be seen in Figure 2.12. With the help of this sequence, and separate receive channels, higher image resolution and higher control on the imaging parameters achieved respectively. One of the two major problems was slice thickness adjustment for the active device and complex anatomical structure visualization at the same time and the other problem remained unaddressed was the localized RF SAR issue [6].

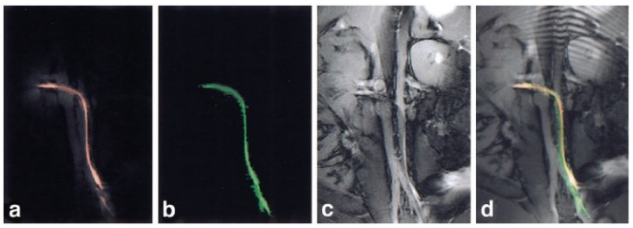

Figure 2.12 In vivo real-time TrueFISP images (a) active guidewire (red), (b) active catheter (green), and (c) surface phased array coils as RF receivers. (d) Overlaid image [6].

2.3.4 Optical Transmission Line Solutions

Long metallic cables used for active device signal transmission or detuning practices during transmission replaced with optical transmission line shown in Figure 2.13 and 2.14 to overcome RF heating related safety issues and design complexity. Photoresistor acts as a switch with its changing resistance by light illumination. Thus

inductively coupled microcoil and tuning capacitors were detuned by light from the fiber optic cable [7].

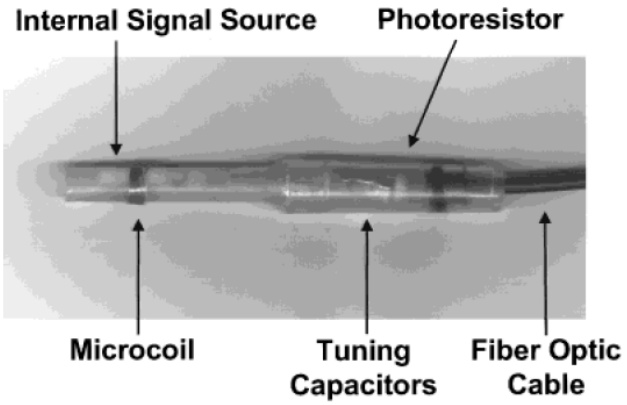

Figure 2.13 Wireless detuning system and schematic of parallel resonant circuits including photoresistor and fiber optic cable. Internal signal source consisting of Gd DTPA-doped saline [7].

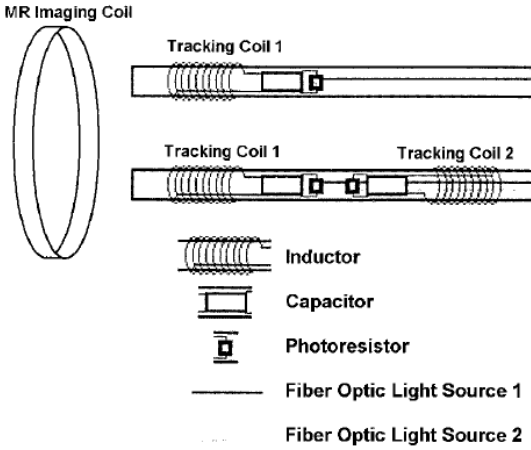

Figure 2.14 Wireless detuning system and schematic of parallel resonant circuits [7].

Another optical approach was developed by [71] in which laser light coupled to an optical fiber, diffused light emitted by photo-voltaic cells, and converted to electrical current in addition to the susceptibility artifacts due to the copper windings. Schematic of the opto-coil approach can be seen in the Figure(2.15). Resulting image is a negative contrast image (dark spot) and made explicit by adjusting the laser power.

For direct optical signal transmission rather than inductively coupled resonant circuits an optical transmission system has been developed. With a resonant circuit connected to a optical transmitter including a transistor and laser diode as in

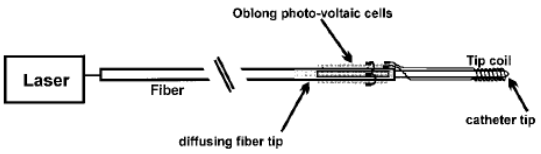

Figure 2.15 Schematic of the Optocoil approach [71].

Figure(2.16), signal was transmitted successfully but with a decreased quality factor (Q-factor) and thus cause degradation in SNR [72]. In the further study, improvements were made regarding SNR which is related to the Q-factor of the receiver microcoil and transconductance (g_m) of the transistor [73].

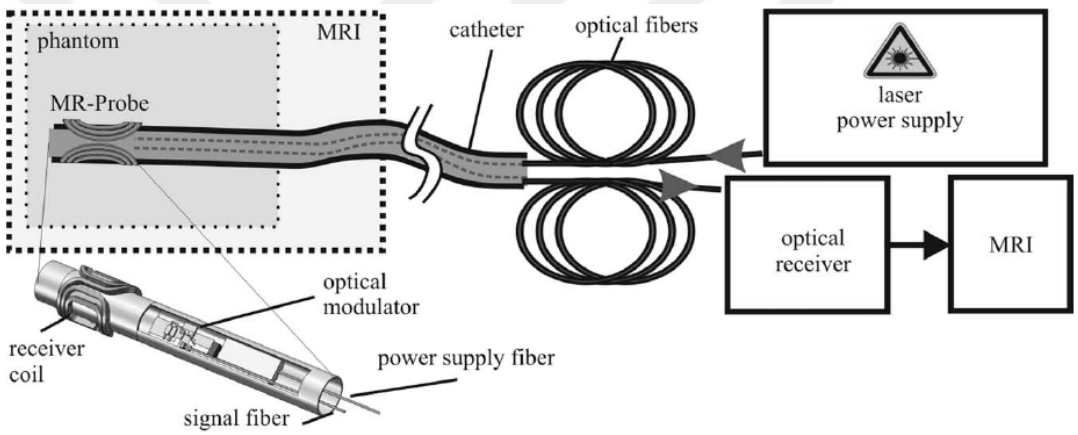

Figure 2.16 Induced voltage times the Q-factor of the resonant circuit produced by the passively decoupled MR micro-Helmholtz coil, transmitted to the optical modulator, optical receiver, and to MRI respectively [73].

There are other optical methods aiming to eliminate RF induced heating such as non-conducting Faraday effect position sensor which detects the position and one orientation angle by using the rotation of the polarization of a light beam relatively with the applied magnetic field applied gradient fields of MRI in one direction. Major disadvantages of the design are stress-induced rotation of the polarization of light which is a misleading factor and inadequate precision in determining the position due to mechanical instability of the sensor. Also the sensor has no ability to transmit the signal thus the method is not useful for imaging purposes [74].

RF related heating concerns gave rise to requirement of E-field measurements.

Owing to the fact that antennas are already electrically conductive themselves, they are not prone those measurements. Hence, optical designs are suitable. Bock.et.al. aimed to measure the E-field and consequently RF heating within the MR by using an electro-optic (EO) sensing principle (Electric field cause change in the polarization which is then detected by the LiNbO3 crystal including sensor) based on the Pockels effect [75].

3. THEORY

3.1 Coil Parameters, and Theory

Inductance of a coil relies on the internal coil parameters and the environment and composed of two components, i.e. internal and external inductance. Those two components depend on the stored energy due to the external magnetic field and coil itself respectively. Internal inductance decreases as the frequency increases because of the skin depth effect. As the frequency increases current tends to flow through the surface of the conductor rather than the inner conductor path. the skin depth formula shown in 3.1 [76].

$$\delta = \frac{1}{\sqrt{f\pi\mu\sigma}} \tag{3.1}$$

In which δ is the skin depth, μ is the magnetic permeability, σ is the conductivity of the wire and f is the frequency.

In order to increase the signal-to-noise ratio (SNR) and thus the sensitivity in the Nuclear Magnetic Resonance (NMR) technique microcoils were the focus since the size of a coil is inversely proportional with magnetic coupling. Taking into consideration of direct relationship between the magnetic flux density (B1) and SNR demonstrated in 3.2 is a proof of smaller the diameter, better the SNR concept [76].

$$\frac{B_1}{i} = \frac{\mu n}{d\sqrt{1 + [\frac{h}{d}]^2}} \tag{3.2}$$

Magnetic flux density and current relationship defined in Ampere's Law can be simplified for the center and both ends of the wire as in 3.3 and 3.4. This is the reason

why the MR bore is the most sensitive area.

$$B = \frac{\mu n i}{h} \tag{3.3}$$

Magnetic flux density in the center of the wire. (while h»r)

$$B = \frac{\mu n i}{2h} \tag{3.4}$$

Magnetic flux density in the ends of the wire. (while h»r)

Hand wound coils [77] provides manufacturing simplicity while more sophisticated micro-fabrication methods used for active and semi-active device tracking and visualization [78].

3.2 MR Microcoils

In Magnetic Resonance Imaging, following the consecutive nonselective RF pulse and three dimensional gradients, spatially changing receive signal obtained [38]. Since microcoils have smaller sensitivity when compared with the RF coil, receive signal from the microcoil obtained as a sharp peak in the frequency domain as demonstrated in Figure(3.1).

Local magnetic field distortions due to the microcoil shifts this peak frequency thus can be misleading. This is also the reason why copper is being used since its magnetic susceptibility is similar to water [79].

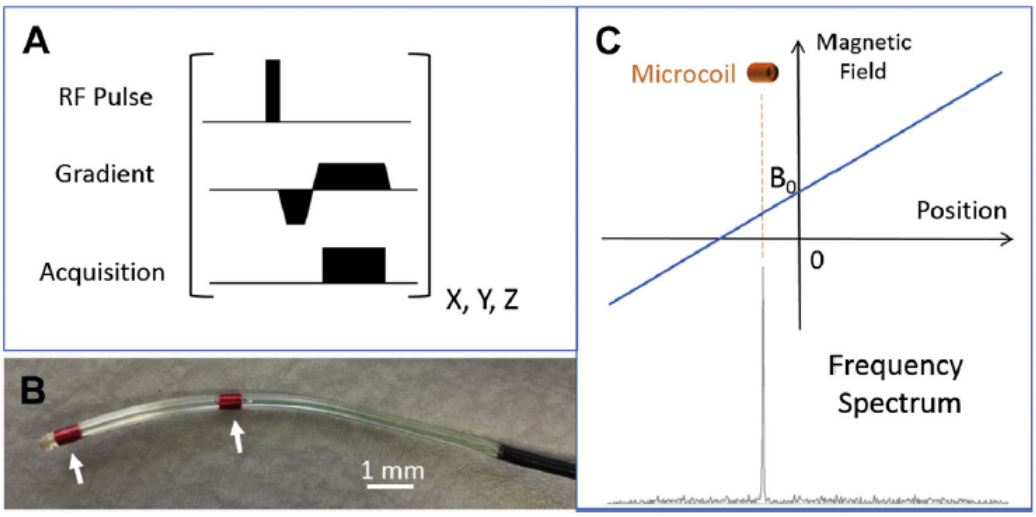

Figure 3.1 MR microcoils (A) MR sequence. (B) A catheter with 2 tracking solenoid microcoils. (C) MR signal received by the microcoil [38].

3.3 Acousto-optic Transmission Line

3.3.1 Optical Fiber Sensors (OFS) and Strain-Optic Effect

Optical signal transmission method had been described first in 1960s and since then is being utilized in diverse areas. Advantages including robustness and sensitivity was listed by underlying principle under OFSs is Acoustic Emission or elastic waves, which can be actively generated by piezoelectric transducers. "The change of refractive index in a material due to an applied strain is called the strain-optic effect." Matrices and relative parameters depicting the strain-optic effect shown in the following equations 3.5, 3.6, 3.7 [80]. Fiber-optic sensors are suitable for various applications since they are insensitive to external factors such as electromagnetic interference and mechanical impacts [81].

$$\Delta(\frac{1}{n^2})_i = \sum_{j=1}^{6} p_{ij} S_j \tag{3.5}$$

Optical indicatrix change is relative to the applied strain in longitudinal axis demonstrated in 3.6 and strain-optic tensor demonstrated in 3.7.

$$S_j = \begin{bmatrix} \varepsilon \\ -\nu\varepsilon \\ -\nu\varepsilon \\ 0 \\ 0 \\ 0 \end{bmatrix} \tag{3.6}$$

$$p_{ij} = \begin{bmatrix} p_{11} & p_{12} & p_{12} & 0 & 0 & 0 \\ p_{12} & p_{11} & p_{12} & 0 & 0 & 0 \\ p_{12} & p_{12} & p_{11} & 0 & 0 & 0 \\ 0 & 0 & 0 & p44 & 0 & 0 \\ 0 & 0 & 0 & 0 & p44 & 0 \\ 0 & 0 & 0 & 0 & 0 & p44 \end{bmatrix} \tag{3.7}$$

in which ε is the applied strain in the longitudinal axis and ν is the Poisson's ratio.

Also, the relationship between the change in the indicatrix and the change in the refractive index described with 3.8.

$$\Delta(\frac{1}{n^2})_{2,3} = -2\frac{\Delta n}{n^3} \tag{3.8}$$

Consequently, refractive index change to applied strain relationship could be derived as depicted in 3.9.

$$\Delta n = -\frac{1}{2}n^3\Delta(\frac{1}{n^2})_{2,3} = -\frac{1}{2}n^3[\varepsilon(1-\nu)p_{12} - \nu\varepsilon p_{11}] \tag{3.9}$$

To be able to detect the strain change with an optical setup, phase and thus

interference change should be described first.

Phase of light ϕ passing through a L length optical fiber calculated as

$$\phi = \beta * L \tag{3.10}$$

In which β is the propagation constant equals to effective refractive index times the wavenumber$(2 * \pi/\lambda)$.

$$\beta = n_{eff} * k_0 \tag{3.11}$$

When we take the derivative of the phase equation and place all the relative parameters in the new equation, phase change can be described by applied strain as shown in 3.12.

$$\Delta\phi = \varepsilon L\beta - \frac{\varepsilon L n^3}{2}[(1-\nu)p_{12} - \nu p_{11}] \tag{3.12}$$

3.3.2 Fiber Bragg Gratings

Fiber Bragg Grating (FBG) is a structure which has a period refractive index composed by an interference pattern embedded in an optical fiber core. FBG acts like an optical filter which reflects only the Bragg wavelength and allows all other wavelengths pass. Bragg wavelength λ_B, is proportional with the effective refractive index n_e, and the grating period Λ and can be demonstrated by the following equation.

$$\lambda_B = 2n_e\Lambda \tag{3.13}$$

To calculate the Bragg wavelength one would need to take the derivation of the Bragg wavelength equation and after required derivations one would reach the final equation shown in 3.14.

$$\Delta\lambda_B = \varepsilon\lambda_B - \frac{\varepsilon\lambda_B n^-}{2}[p_{12} - \nu(p_{12} + p_{11})] = \varepsilon\lambda_B(1 - \frac{n^2}{2}[p_{12} - \nu(p_{12} + p_{11})]) \quad (3.14)$$

3.3.3 Piezoelectric Transducers for Ultrasound Applications

Piezoelectric transducers have been a preferred solution especially for ultrasound imaging applications. Higher electromechanical coupling values should be reached to enhance the sensitivity. Another important parameter describing the performance of a transducer is the Acoustic Impedance. The acoustic impedance difference (mismatch) between human tissue ($\approx 1.5kg/m^2 - s$) and PZT ($\approx 30 * 10^6 kg/m^2 - s \approx 30Mrayl$) specifies the performance in other words quality factor of the transducer [82].

In order to obtain acousto-optic signal transmission, a piezoelectric transducer coalesced with the fiber bragg grating (FBG). Piezoelectric effect was discovered in 1880 by Pierre and Jacques Curie and defined as electric field composition due to an applied stress to a quartz crystal. Reciprocally electric field composition causing mechanical deformation in a quartz crystal [83]. Lead-Zirconate-Titanate (PZT) metallic composition generates a high internal dipole moment thus defines them as ferroelectric material and the critical transition temperature defines their stability as well. Figure(3.2) showing properties of different transducers, especially acoustic impedance for matching, and high piezoelectric coupling factor for energy storage should be taken into consideration regarding design efficiency [83]. The thickness of the piezoelectric transducer is considerably smaller than the length and width, when applied to an external stress, significant amount of displacement occurs only in one direction which provides high sensitivity. Piezoelectric transducer Strain-Electric field relationship can be written in the following equation:

$$S = dE \tag{3.15}$$

In 3.3 S is strain, d is piezoelectric strain constant and in the polarized direction it can be expressed as d_{33} and E is the electric field. For the polarized direction 3.3 can be rewritten as:

$$\varepsilon_e = d_{33}\frac{U}{M} \tag{3.16}$$

In this case, U is the drive voltage and M is the distance between the electrodes of the PZT.

Since electrical to mechanical and reverse conversion takes place within the transducer, Strain (S), Stress (T), Charge density (D), and Electric field (E) relationships should be defined as demonstrated in Figure(3.3). Superscripts in the equations in Figure(3.3) shows parameters was hold constant and subscripts show the crystal lattice notations and directions in three dimension.

Property	Thickness Expansion Parameters	Units	PZT4	PZT5A	PZT5H	Lead Metaniobate	PVDF
Speed of Sound	c_T	m/s	4600	4350	4560	3200	2000
Density	ρ	10^3 kg/m^3	7.5	7.75	7.5	6.2	1.8
Acoustic Impedance	Z_0	10^6 Rayl	34.5	33.7	34.2	20.0	3.4
Elastic Compilance	c_{33}^D	10^{10} N/m^2	15.9	15.9	14.7	–	0.95
Dielectric Constants							
[a] free	$\epsilon_r^T = \epsilon_{33}^T/\epsilon_0$	unitless	1300	1700	3400	–	
[b] clamped	$\epsilon_r^T = \epsilon_{33}^S/\epsilon_0$	unitless	635	830	1470	300(266)[b]	8@3.5 MHz
Piezoelectric Constants							
[a] e	e_{33}	C/m^2	15.1	15.8	23.8	–	0.06
[b] h	h_{33}	10^8 V/m	26.8	21.5	18.4	–	53[a]
[c] d	d_{33}	10^{-2} C/N	289	375	593	85	17.5[a]
[d] g	g_{33}	10^{-3} V · m/N	25.1	24.9	19.7	32	174[a]
Piezoelectric Coupling Factor							
[a] free (no lateral restraint)	k_{33}^I	unitless	0.70	0.70	0.75	–	–
[b] clamped (lateral restraint)	k_{33}^t	unitless	0.51	0.49	0.50	0.32	0.2
Reference for Suppliers			115	115	115	37	117

Figure 3.2 Properties of Different Piezoelectric Transducers [83].

Pressure waves generated on the back and front electrodes of transducers shown in Figure(3.4) also time dependent reverberations within the transducer takes place.

Piezoelectric Constant	Electrical Relationships	Mechanical Relationships
d	$D_j = d_{jp}T_p + \epsilon^T_{ji}E_i$	$S_q = S^E_{pq}T_p + d_{jq}E_j$
e	$D_j = e_{jp}S_p + \epsilon^S_{ji}E_i$	$T_p = c^E_{pq}S_q - e_{jp}E_j$
g	$E_j = -g_{jp}T_p + \beta^T_{ij}D_i$	$S_q = S^D_{pq}T_p + g_{jq}D_j$
h	$E_j = -h_{jp}S_p + \beta^S_{ij}D_i$	$T_p = c^D_{pq}S_q - h_{jp}D_j$

Figure 3.3 Piezoelectric constants defined by the four related parameters [83].

Frequency of a transducer calculated by the speed of sound divided by the thickness of the transducer.

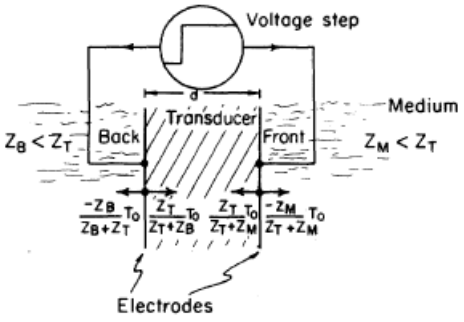

Figure 3.4 Schematic of pressure wave generation when applied voltage to a transducer [83].

Taken into consideration above equations expressing the PZT and FBG working principle, a change in the applied voltage hence the electric field result in the strain change in the PZT and cause refractive index and Bragg wavelength change in the FBG region in turn. This is also applicable in our design, composed electric field in the MR environment can be measured by recording the refractive index and Bragg wavelength change in the FBG [84].

3.3.4 Crosstalk between Piezoelectric Transducer and the Electromagnetic Field

Intermetallic composition of the PZT transducers causes a crosstalk with the RF excitation and thus electromagnetic field composing surrounding the transducer. This interaction including the acoustic pressure occurring on the transducer derived in

[85] as in 3.17 and 3.18.

$$p(t) = \frac{1}{2} B_0 \rho_s c[\Delta(\frac{\sigma}{\rho})] g_x Q(t)(Pascal) \tag{3.17}$$

$$Q(t) = \int_{-\infty}^{t} E_0(t')dt', \tag{3.18}$$

where ρ_s is the mass density, c is the speed of sound in saline, g_x is the spatial information and σ is the conductivity.

It should be noticed that E_0 is taken only time dependent which due to the quasistatic approximation. Considering the two equation above and the transmitting sensitivity of the transducer ($\frac{Pa}{V}$) one would conclude the voltage generating on the transducer. This generated voltage can be seen as noise and need to be shielded since this would add an additional strain effect on top of the desirable measure

3.3.5 RF Transmit Coil and Piezoelectric Transducer Coupling

Underlying principle of electrical signal from the distal loop coil to acoustical signal generated by the ultrasonic transducer transmission is well-known "Faraday's Law of Induction" which is expressed in the 3.19 below;

$$V_{ind} = -N\frac{d\phi}{dt} = -N\frac{d(BA)}{dt} \tag{3.19}$$

Induced voltage by Faraday's Law should be multiplied with the Q-factor of the coil as depicted by [74].

3.4 RF Shielding Theory and Material Selection

As explained in Section 3.3.4, a cross-talk between RF transmission pulses and ultrasound transducer occurs during MRI scan and this needs to be eliminated. Underlying principle of radio frequency field shielding is based on both reflection and absorption mechanisms of shielding materials. Reflection occurs due to the generated currents due to varying electric and magnetic fields. Time varying electric fields induce electric displacement current opposing the electric field and related Maxwell equation can be seen in 3.20. Similarly, varying magnetic fields compose eddy currents which opposes the magnetic field and related Faraday's Law of Induction equation can be seen in 3.21.

$$I_d = \varepsilon_0 \frac{d\Phi_E}{dt} \tag{3.20}$$

$$\varepsilon = -\frac{\Delta\Phi_m}{\Delta t} \tag{3.21}$$

Underlying principle of absorption mechanism is the skin effect. In conductive materials, current tends to flow through the surface which can also be explained by the skin effect. Taking into account the skin depth formula given in 3.26, inverse relationship between the conductivity, permittivity, magnetic permeability and skin depth can be seen. In Figure(3.5), shielding mechanism including the reflection, absorption and re-reflections within the material was demonstrated and shielding effectiveness calculation can be seen in 3.22 [9].

$$SE_{dB} = R_{dB} + A_{dB} + B_{dB} \tag{3.22}$$

Highly conductive material would be a reasonable choice in order to provide an efficient shielding. A preliminary study was performed using a polymer composite

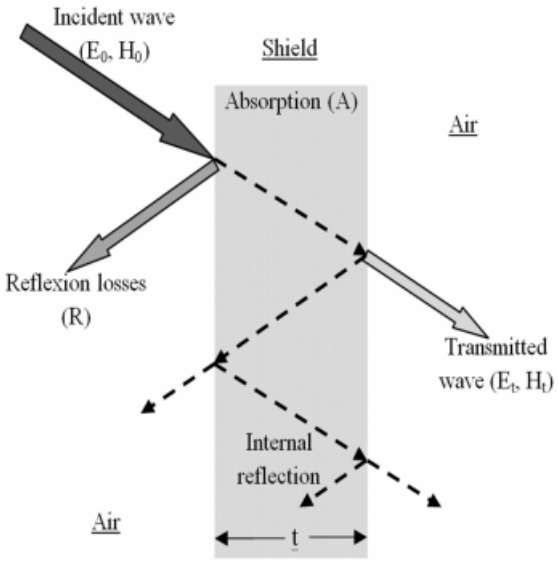

Figure 3.5 EMI shielding mechanism [9].

which is copper-epoxy mixture to shield the ultrasound transducers used in Ultrasound/MRI fusion imaging [86]. The reason for copper as the metallic element is that its relatively high conductivity and its relatively close magnetic permeability value to human body and thus creates smaller artifact in the acquired MR image. Also copper is an abundant and low cost material. However one challenge that complicates the use of copper is the surface oxidation. This problem can be overcomed by using epoxy material. Sintered metal particles are constituting the conductive inks and adhesives which are commonly used in electronics.

One of the most important concern during MR Imaging is the image distortions and RF safety related issues due to the eddy currents. Thus, eliminating the eddy current generation and transducer insulation at the same time requires a capacitor like behavior. Since diamagnetic materials (i.e. silver,copper and gold) are less susceptible to external magnetic field, therefore suitable for MR applications. Aluminum-epoxy composite was investigated by [87], and it was found that the composite behaves like a capacitor in such a way that in high frequencies, impedance decreases and thus material becomes conductive. Polymer composites like Copper-epoxy or Aluminum-epoxy composites creating conductive paths in the structure and attenuating the incident waves are convenient for this application [86, 87, 8].

3.5 Different Methods for Shielding Effectiveness (SE) Measurements

Shielding effectiveness which represents the reflectivity and attenuation can be calculated in 3.23 and can be measured by different methods which can be categorized as Transverse Electromagnetic (TEM) cell methods (ASTM-4935 standardized SE measurement) and Free space methods including different antenna types [9]. TEM cell method as described in the ASTM-4935 standard [88], is based on capacitive coupling of the flanged outer conductors and the shielding material, thus flanges of the outer conductor should not touch each other. The major difficulty is to prepare load and reference samples in a specific thickness and geometry and thus implementation is difficult. On the other hand, measurement is not effected by the external perturbations. Coaxial transmission line included measurement setup is demonstrated in Figure(3.6). A TEM cell and a TEM-t cell can be seen Figure(3.7) with load and reference samples [8],[9].

$$SE(decibels, dB) = 10 \log \frac{P_i}{P_o} \tag{3.23}$$

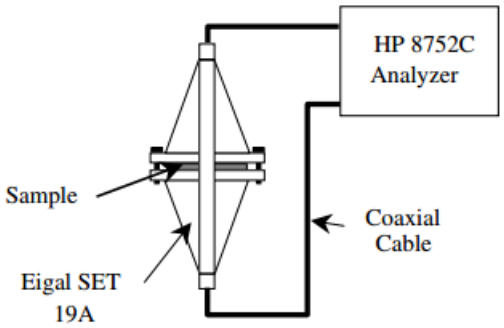

Figure 3.6 Setup for EMI SE testing in transmission and reflection [8].

Free space methods are based on antennas with different configuration used in transmit and receive modes to measure the shielding effectiveness. In these methods, in order to eliminate the external perturbations, anechoic chambers which absorb the incident waves can be used similarly to TEM cells which is demonstrated in Figure(3.8).

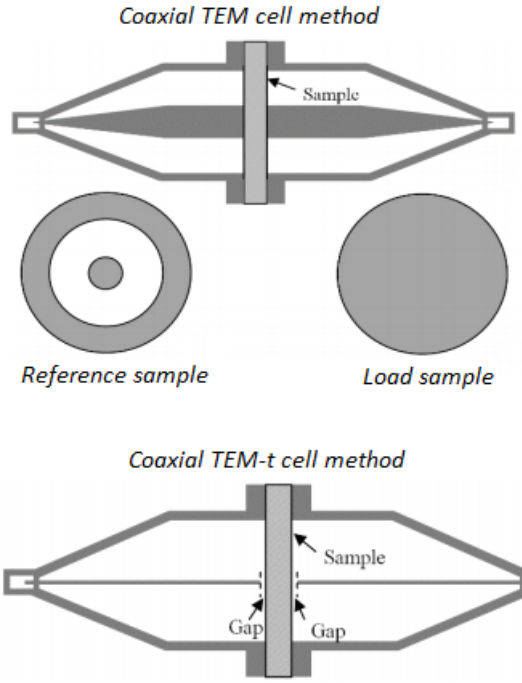

Figure 3.7 Demonstration of coaxial TEM cell (ASTM4935-10) and coaxial TEM-t cell [9].

An applicable configuration including loop antennas and a measurement sample placed in between can be seen in Figure(3.9).

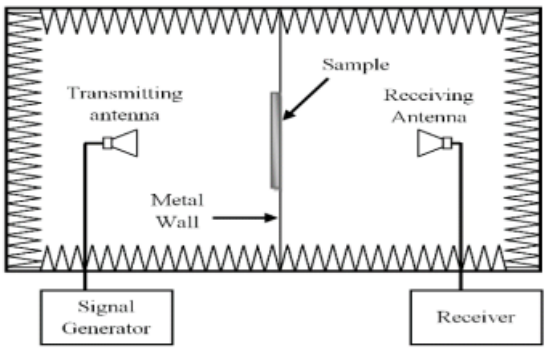

Figure 3.8 Shielding effectiveness measurement in an anechoic chamber [9].

3.6 Antenna Theory and Monopole Antennas

A conductive wire in a particular electrical length acts as an electromagnetic wave radiating antenna. Quarter wavelength monopole antennas are commonly used

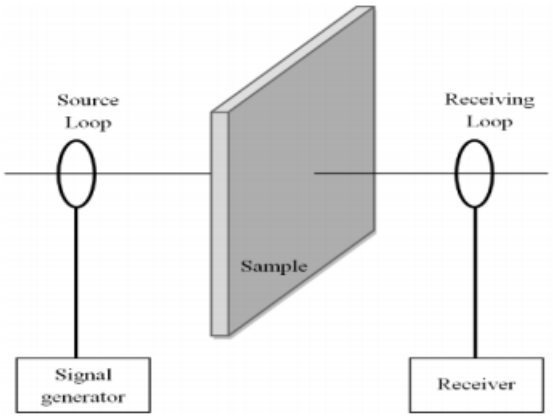

Figure 3.9 Shielding effectiveness measurement with loop antennas and the sample placed in between [9].

type of monopoles in which antenna length equals to the $\frac{1}{4}$ of the wavelength.

Monopole antennas with a circular ground plane can be described with several parameters i.e. antenna length, antenna radius, and ground plane radius and dielectric constant and loss tangent of the environment as well. Antenna ground can be selected as highly conductive metal such as pure copper material and the ground length and height should be larger than the quarter wavelength. Antenna excitation described with a time dependent equation $\exp jwt$ at a radial frequency $w = 2\pi f$ $(\frac{rad}{sec})$ and free-space wavelength $\lambda = \frac{c}{f}$ where c is the free-space velocity of light [89]. Loss tangent δ is calculated by;

$$\tan\delta = losstangent(dissipationfactor) = (\frac{\sigma}{\omega\varepsilon_0\varepsilon_r}) = (\frac{60\lambda\sigma}{\varepsilon_r}) \tag{3.24}$$

Radiated power P_r radiated is calculated by;

$$P_r = (\frac{\pi}{Z_0}) \int_0^{\frac{\pi}{2}} IE_\theta(r,\theta) I^2 r^2 \sin\theta d\theta, \tag{3.25}$$

"Skin depth δ refers to the depth in earth at which the electromagnetic field has attenuated to $\frac{1}{e}$ of its value on the underside surface of the earth." Skin depth δ is

calculated by;

$$\delta_s = [(\frac{\omega^4 {\mu_r}^2 {\varepsilon_r}^2}{4c^4}) + (\frac{\sigma^2 \omega^2 {\mu_r}^2 {\mu_0}^2}{4})^{\frac{1}{2}} - (\frac{\omega^2 {\mu_r}^2) {\varepsilon_r}^2}{2c^2}]^{\frac{-1}{2}} \tag{3.26}$$

A monopole antenna demonstrated in Figure(3.10) can be thought as if it is twice as long as a dipole antenna and thus the input impedance of the monopole antenna equal to one-half of the dipole antenna if the ground is taken as infinitely large. In reality, finiteness of the ground plane should be taken into consideration. In fact, larger the ground plane, smaller the impedance mismatch but give rises to environmental diffraction which in turn causes distortion of the radiation pattern [90].

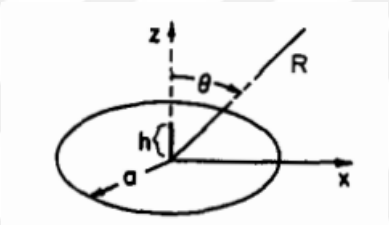

Figure 3.10 Monopole on a circular disk [90].

3.7 Phantom Formulation and ASTM F2182-09 Standard

ASTM $F2182-09$ Standard Test Method for Measurement of Radio Frequency Induced Heating On or Near Passive Implants During Magnetic Resonance Imaging [96], is a standard method to test implants in a phantom material that simulates the electrical and thermal properties of the human body. The phantom material is a gelled saline consisting of a saline solution and a gelling agent. Gelling agent is required in order to increase viscosity thus prevent phantom allow convective heat transfer [32].

Phantom container should not be selected as a conductive material and can be made of i.e. Poly(methyl methacrylate) which is a highly insulating material. Suggested gelled saline mentioned in the related standard can be prepared by using specific

ratios of sodium chloride (NaCl) and polyacrylic acid. By using this formulation close conductivity (0.47 S/m) and relative permittivity (77) of human tissue can be obtained.

3.8 Wavelength Calculation of Monopole Antennae in Phantom

Wavelength of an EM wave in free space can be calculated as $\lambda = \frac{v}{f}$ in which phase speed (v) equals to the speed of light ($c = 3 * 10^8 m/s$) and f is the frequency of the electromagnetic wave. If the environment is different than vacuum, then dielectric constants, magnetic permeability and conductivity of surrounding environment should be taken in to consideration. Thus a more complicated wavelength calculation as in 3.27 derived in [91]. Electrical and thermal properties of tissue mimicked by a well-prepared phantom as described in the ASTM $F2182 - 09$ test method [32].

$$\lambda = \frac{2\pi}{\omega\sqrt{\frac{\mu\varepsilon}{2}}\sqrt{1 + (1 + \frac{\sigma^2}{\omega^2\varepsilon^2})^{\frac{1}{2}}}} \tag{3.27}$$

3.9 Design Concept

In the proposed design, RF induced active device heating and developing a conspicuous MRI catheter design problems planned to overcome with a clinical-grade active guiding catheter device that does not need long conductor transmission lines for active device visualization under MRI. The active guiding catheter design incorporates a distal loop coil that is electrically connected to an ultrasonic transducer having a comparable profile. The ultrasonic transducer converts the electrical input from the coil to elastic waves at one end of an optical fiber with an embedded interferometric detection structure (a fiber Bragg grating). The elastic waves over the grating result in acousto-optical modulation of the grating which is detected by a laser coupled to the proximal end of the optical fiber that runs along the active catheter shaft. Therefore,

the received RF signal through the distal loop antenna can be transmitted through using a RF heating free, dielectric transmission line to the MR scanner for device visualization purpose. The schematic of the test setup demonstrated in Figure(3.11).

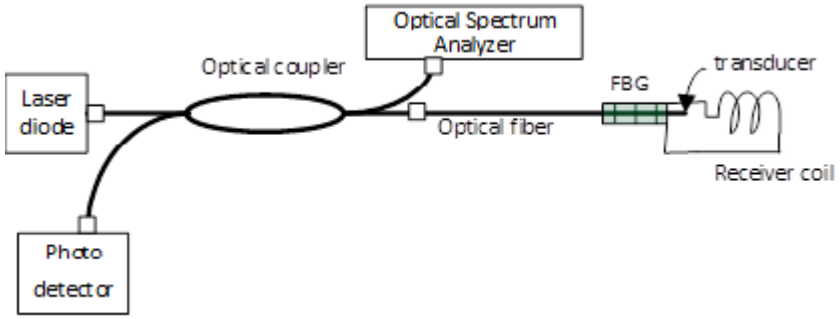

Figure 3.11 Schematics of the test setup including the active receiver with coupled acousto-optic modulator transducer and optical fiber transmission line with FBG.

4. METHODS

In this chapter simulation and experiment methods will be presented. First, monopole antennas with ground plane modelled within the phantom environment in $CST^{®}$ software. Three different RF shielding materials in planar geometry were placed between the monopole antennas. Also, one of the monopole antennas was surrounded by three different shielding materials in cylindrical geometry. Following the simulation steps, experiment setup was described including the shielding materials (copper tape, copper powder-epoxy mixture, conductive silver ink) and geometries (planar and cylindrical), wavelength calculation for monopole antennas, antenna and ground plane construction, phantom container construction, phantom preparation and electrical conductivity measurements.

4.1 Simulation Design Methodology

The phantom experiment setup simulations was performed in $CST^{®}$ (Computer Simulation Technology AG., Dassault Systems) program which is an Electromagnetic simulation software. In CST it is possible to design and test electromagnetic behaviors of designed components. In particular, CST MICROWAVE $STUDIO^{®}$ ($CST^{®}$ $MWS^{®}$) "Antennas" tool was used for this high frequency application.

Simulation Parameters and material properties are shown in Table 4.1 and Table 4.2 respectively. Dimensions of the ground plane (made of 0.5 mm thick pure copper plate) equals to constructed ground plane dimensions which can be seen in Figure(4.9). Monopole antennas (both for copper made and coaxial cable made) were designed in CST, inner conductors of the coaxial cables were inserted into the phantom and excitation ports were placed at the both ends of the coaxial cables. Phantom container was not described in the simulation since it was an insulating polymer material. However, gelled phantom material with its measured conductivity value and permittivity value described in [32] was simulated. Finally, different shielding materials including copper

tape, copper powder-epoxy blend and flexible conductive ink were simulated. Copper tape was selected from the material library of the program itself, but copper powder-epoxy mixture relative permittivity value which is approximately 15 was acquired from the literature [93]. Surface resistivity value is order of magnitude smaller than the annealed copper, thus the electrical resistivity value of the mixture was inserted as $5 * 10^{-8}$. Other properties such as relative magnetic permeability, mass density, thermal conductivity, Young's modulus, Poisson ratio and thermal expansion coefficients were hold same as the annealed copper. Conductive silver ink was also selected from the material library of the program.

In this design, antenna lengths (inner conductor of the coaxial cable) in the phantom container was chosen as quarter wavelength and the distance between the antennas was set to 5 cm which is approximately half of the effective antenna lengths. Excitation ports (Port 1 and Port 2) were placed at the end of the outer part of the coaxial cable as in the experimental set-up. Since the impedance of the coaxial cable is directly relevant with the thickness of the inner conductor, outer conductor and the dielectric material($\varepsilon_r = 2.3$) in between, we need to know the precise diameters. For the accurate simulation of the monopole antennas made of coaxial cables (RG-58) their dimensions were first verified with a microscope (Hirox Microscope KH 8700) and the measured dimensions are shown in Figure(4.1.

Table 4.1
CST Simulation parameters including coaxial cable antenna dimensions, different shielding materials (copper and silver) and geometries (plane and cylindrical).

	Outer radius(cm)	Inner radius(cm)	Width(cm)	Height(cm)	Length(cm)
Inner Conductor - Aluminium	0.04	0			112
Outer Conductor - Aluminium	0.16	0.14			101
Dielectric Material - LDPE	0.14	0.04			101
Phantom (Gelled Saline)			16	8	20
Plane Shielding			0.05	4	14
Cylindrical Shielding	0.25	0.2			14

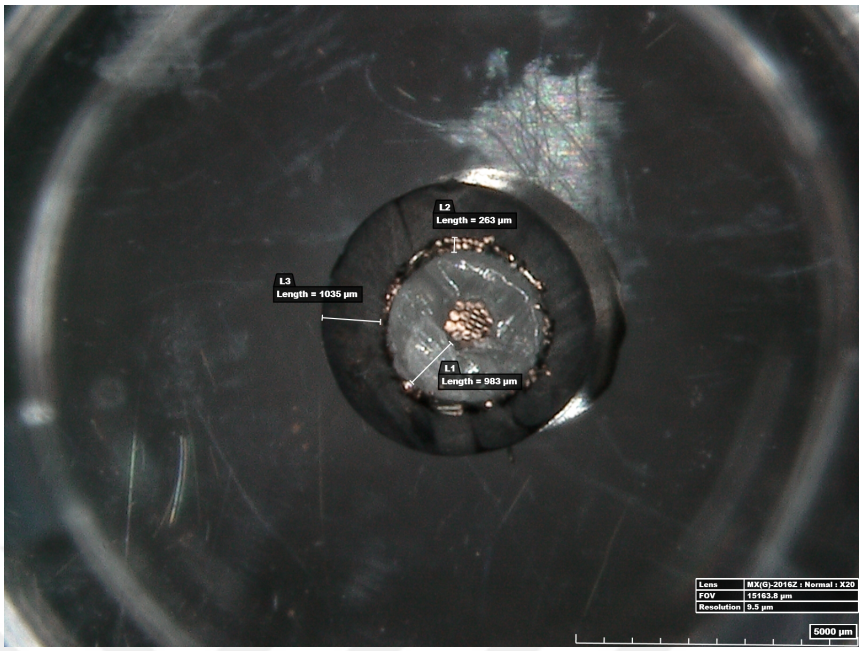

Figure 4.1 Microscopic (Hirox Microscope KH 8700) cross-section view of RG-58 coaxial cable(Lens MX(G)-2016Z: Normal: X20, FOV: 15163.8 μ m , Resolution: 9.5 μ m).

3D demonstrations of experiment set-up simulated in CST software are shown in Figure(4.2) and Figure(4.3).

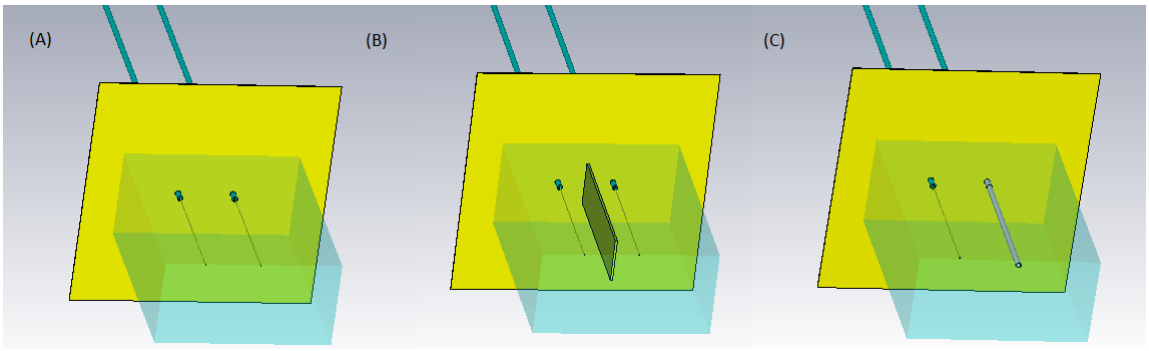

Figure 4.2 (A) 3D demonstration of phantom with no shield. (B) 3D demonstration of phantom with plane copper shielding. (C) 3D demonstration of phantom with cylindrical silver shielding.

4.2 Experiment Setup for the Shielding Measurements

To measure the shielding property of different materials, one would need to set a measurement set-up including antennas radiating electromagnetic waves. S-parameter (Scattering parameters) matrix is being used to measure the reflected and incident

Table 4.2
Electrical conductivity (S/m) and density (kg/m^3) defined in CST as the material parameters.

Parameters	Conductivity (S/m)	Density (kg/m^3)
Aluminium (lossy metal)	3.56x10^7	2700
Phantom (Gelled saline)	0.47	1025
Copper (lossy metal)	5.80x10^7	8930
Silver (lossy metal)	6.30x10^7	10500

wave voltages. While S_{11} and S_{22} indicate the reflection coefficients, S_{21} represents the forward transmission coefficient [94]. Thus shielding can be measured using S-parameters of antennas connected to the vector network analyzer shown in Figure(4.4).

4.2.1 Shielding Material and Geometry

In this study, three different materials which are copper powder-epoxy mixture (CuPro-Cote^{TM} Coating), silver conductive ink (AG-594 Flexo-Printable Silver Conductive Ink, Conductive Compounds) and copper tape with two different geometries (plane and cylindrical) were examined as a shield which are shown Figure(4.7). Epoxy is a widespread and cost-effective material in industrial applications and mixing with conductive particles inhibits the oxidation of the metal particles [95]. Silver has a close electrical conductivity value as copper. Due to its convenience and being a cost-effective solution, a printible silver conductivity ink including silver particles was selected.

Electrical resistivities ($\Omega.m$) of reference annealed copper (lossy metal), conductive silver ink and copper-epoxy blend are demonstrated in Table(4.3).

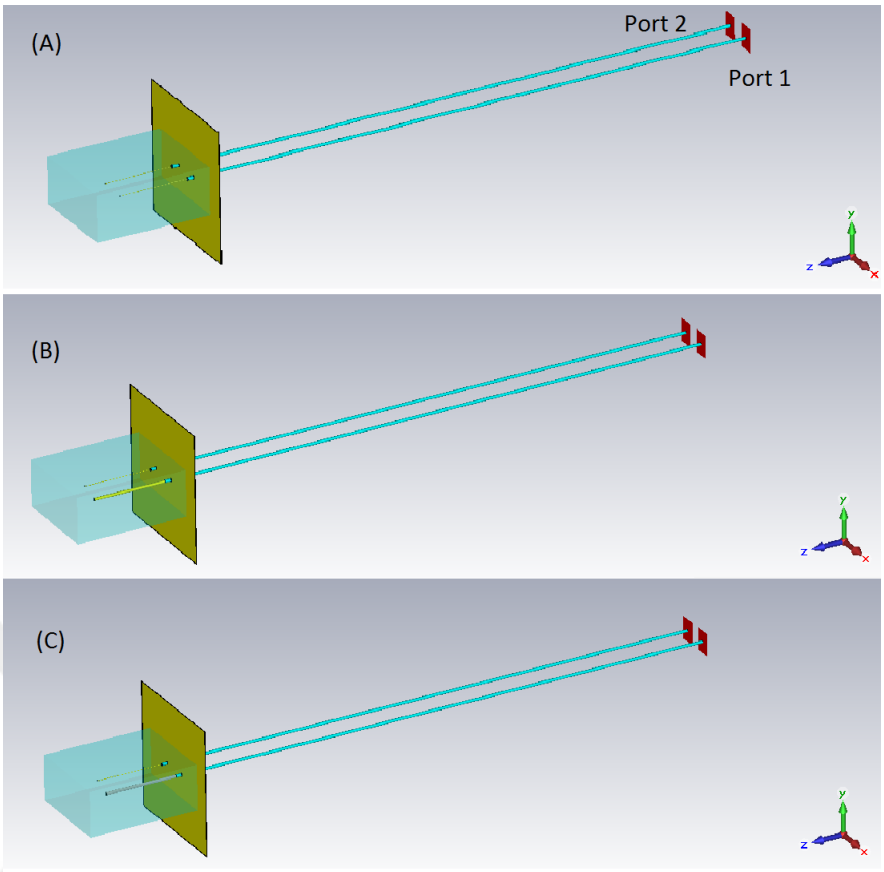

Figure 4.3 (A)3D demonstration of phantom with no shield. (B)3D demonstration of phantom with cylindrical copper shielding. (C)3D demonstration of phantom with cylindrical silver shielding.

4.2.2 Wavelength Calculation in Phantom

In theory, for a dipole antenna resonance occurs when the antenna length equals to the half-wavelength [32] and reactance becomes zero [94]. A complex wavelength equation as in 4.1 was used to calculate the wavelength while taking into account the relative permittivity, permeability and conductivity of the phantom. MATLAB code for the wavelength calculation can be found in the [Appendix A].

$$\lambda = \frac{2\pi}{\omega\sqrt{\frac{\mu\varepsilon}{2}}\sqrt{1+(\frac{\sigma^2}{\mu^2\varepsilon^2})^{\frac{1}{2}}}} \tag{4.1}$$

in which relative permittivity (ε_r) equals to 77, and conductivity (σ) equals to 0.47 S/m. After substituting the constants in the formula, wavelength was calculated

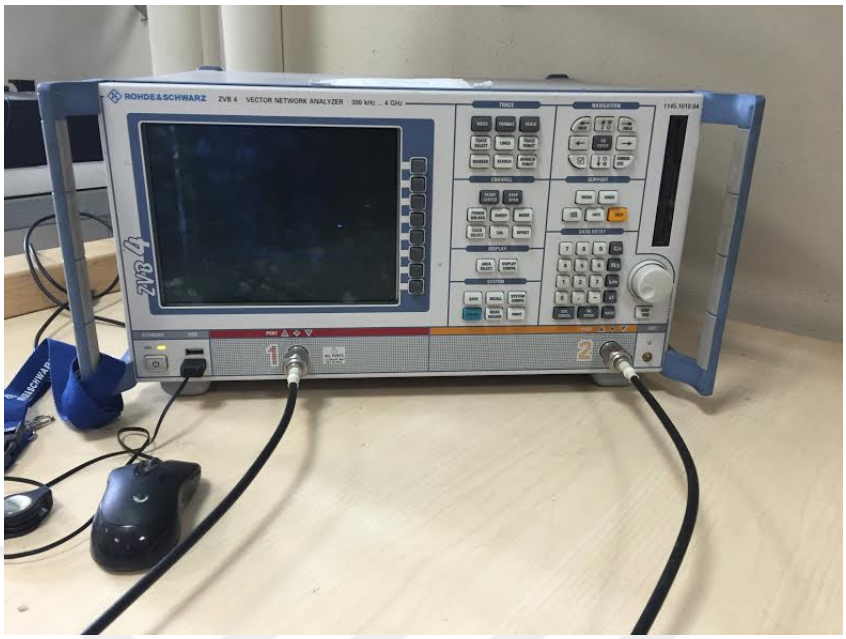

Figure 4.4 Rohde and Schwarz ZVB4-Vector Network Analyzer

Table 4.3
Electrical resistivity values of different RF shielding materials ($\Omega.m$)

Shielding Materials	Resistivity ($\Omega.m$)
Copper (lossy metal)	$1.72 * 10^{-8}$
Copper powder-epoxy mixture	$5 * 10^{-8}$
Conductive silver ink	$1.59 * 10^{-8}$

as approximately 44 cm.

4.2.3 Antenna and Ground Plane Design and Construction

Monopole antenna can be identified as the half of a dipole antenna. In fact, length of the monopole antenna equals to $\frac{\lambda}{4}$ which is the half of the length of a dipole antenna. Also, it is important to note that power radiated from the monopole antenna and the input impedance are half of the dipole antenna. For this project, monopole antenna was selected for its manufacturing convenience. The common ground plane was selected as copper since copper has high conductivity. Commercial coaxial cables

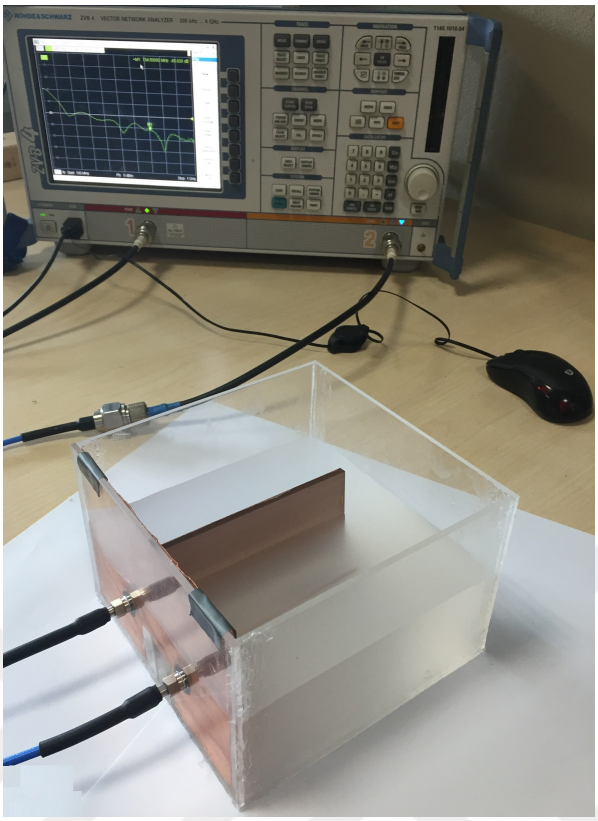

Figure 4.5 Phantom filled PMMA container including the copper-epoxy plane shield placed between the monopole antennas connected to Rohde and Schwarz ZVB4-Vector Network Analyzer

(RG-58) were used in construction of monopole antennas. Coaxial cables were arranged as 100 cm of the insulated part had kept outside of the phantom and after stripping off the outer conductor, inner conductor (11 cm length) inserted into the phantom which is equal to $\frac{\lambda}{4}$. Inner conductors of the coaxial cables which were inserted into the phantom container is demonstrated in Figure(4.8).

Ground plane was selected from a commercial pure ($platethickness = 0.5mm$) copper plate and was cut in order to fit the SMA connected monopole antennas and its dimensions was adjusted according to the phantom container dimensions as shown in Figure(4.9). An aperture was left intentionally, this was because of the mold (for planar shielding placements) at the container base.

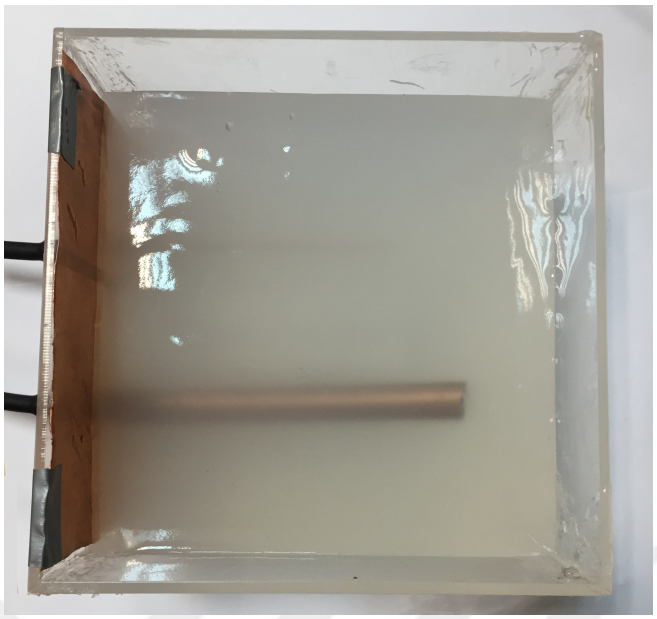

Figure 4.6 Phantom filled PMMA container including the copper-epoxy cylindrical shield placed between the monopole antennas

4.2.4 Phantom Preparation

As shown in previous study [96], phantom container should be made of an insulator material. Thus, for manufacturing convenience and availability, poly (methyl methacrylate) was used as the phantom container material and monopole antennas in different configurations were measured within this phantom container. Container dimensions are as following, Length: 15 cm, Width: 15 cm, Height: 10 cm.

RF induced heating and safety tests for MR compatible medical grade devices are performed within a tissue mimicking gelled saline described in the ASTM standard [96]. According to the ASTM F2182 – 09, gelled saline (phantom) which has similar electrical properties as tissue can be made with 10 g/L polyacrylic acid(PAA), 1.32 g/L NaCl and deionized water. First PAA and NaCl are weighted by Analytical Balance (*Cubis*® - Sartorius) for one liter solution. 100 mL deionized water was stirred to dissolve the 1.32 g NaCl completely and then remaining deionized water was added and was stirred to mix. 10 g PAA was added to the solution a bit at a time, was stirred to suspend completely. After each addition, a kitchen grade immersion blender with a blade was used to distribute and dissolve completely. The blender is turned on

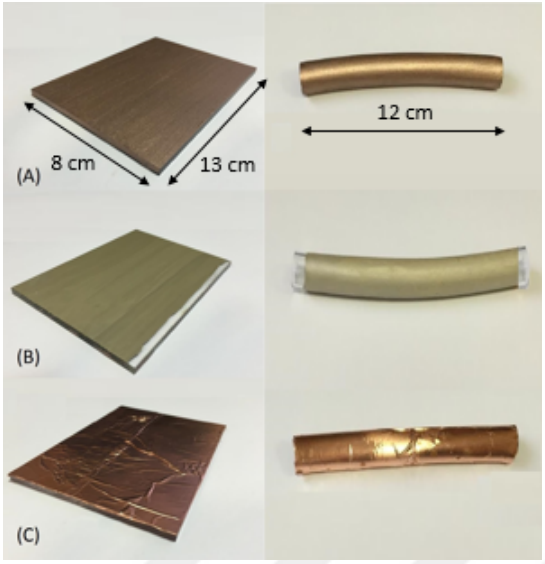

Figure 4.7 Different shielding materials applied on plane PMMA demonstration. (A) Copper powder-epoxy mixture. (B) Silver conductive ink. (C) Copper tape.

intermittently for at least 20 min total in order to remove all lumps of any discernable size. Phantom was put in the dessicator in order to remove the formed air bubbles during the process as in Figure(4.10). Phantom was ready to use after 24 hours waiting-period. The appearance of the slurry should be semi-transparent, free of bubbles, and free of lumps of any discernible size. Conductivity should be verified in the later stage.

4.2.5 Electrical Conductivity Measurement

In order to well mimic the tissue properties, one would need to satisfy the phantom specifications. Thus, one of the most important parameter which is the conductivity of the prepared phantom according to the ASTM F2182 – 09 should be between 0.47 ± 10 S/m at 64 MHz and 128 MHz [32, 96]. Conductivity is an indicator showing the ions within the solution and its unit is S/cm which is calculated by the Conductance (S) times the cell constant (cm^{-1}). In this study, Lutron CD-4303HA Conductivity Meter were used for the conductivity measurements. Acquired conductance values shown in Figure(4.11)are between 4.78 mS and 5.00 mS and S/cm values are calculated as between 0.478 S/cm and 0.5 S/cm taking into consideration that the distance between electrodes within the conductivity meter is 1 cm.

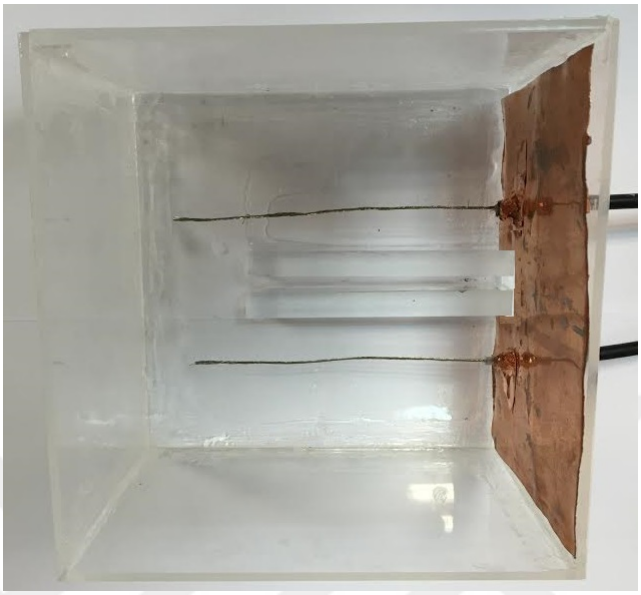

Figure 4.8 Stripped coaxial cables were inserted into the phantom container.

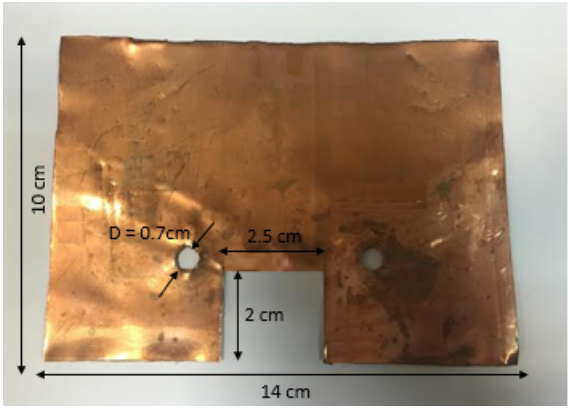

Figure 4.9 Ground plane for monopole antennas made of pure copper plate.

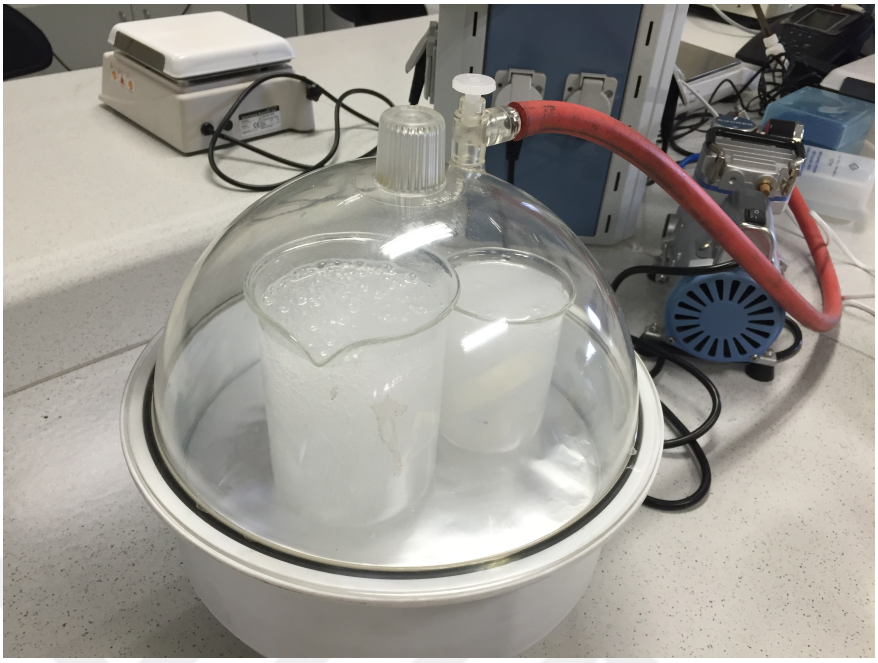

Figure 4.10 Phantom was put in the dessicator to remove the air bubbles.

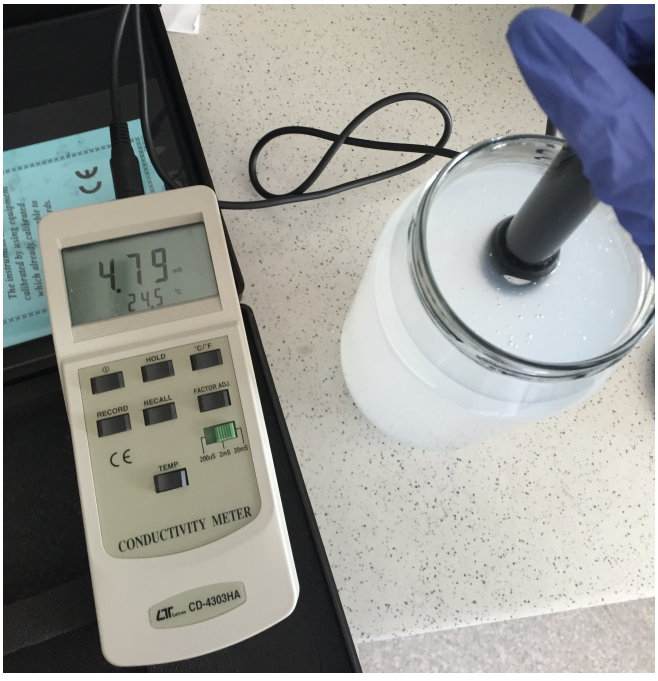

Figure 4.11 Conductivity measurement of phantom.

5. RESULTS

In this chapter simulation and experimental results will be presented.

5.1 Simulation Results

Simulations were performed within the frequency range of 50 MHz to 900 MHz and S-Parameters were analyzed within this frequency range. S_{11} and S_{21} parameters without any shielding material are shown in Figures(5.1, 5.2), S_{21} parameters with plane and cylindrical geometries for both copper (both copper tape and copper powder-epoxy blend) and silver shielding materials are shown in Figure(5.3, 5.4, 5.5, 5.6, 5.7 and 5.8).

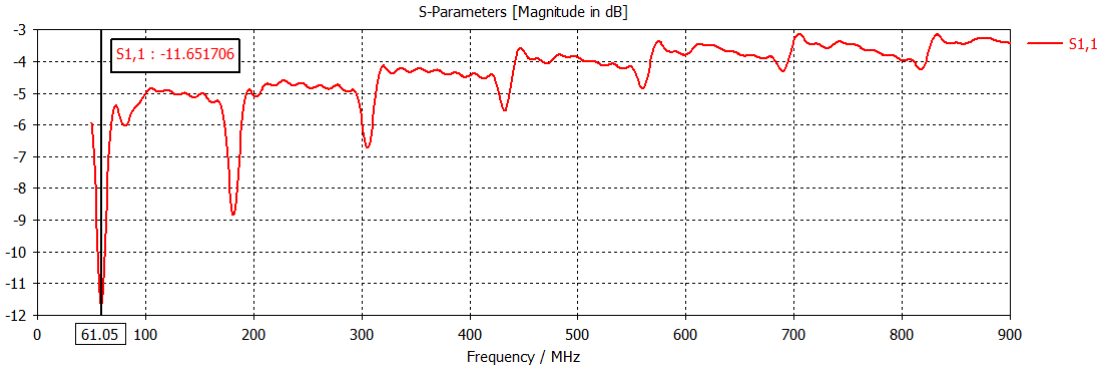

Figure 5.1 S_{11} parameter demonstrating the antenna behavior without any shielding material (The Black marker shows that S11 is -11.6 dB at 61 MHz).

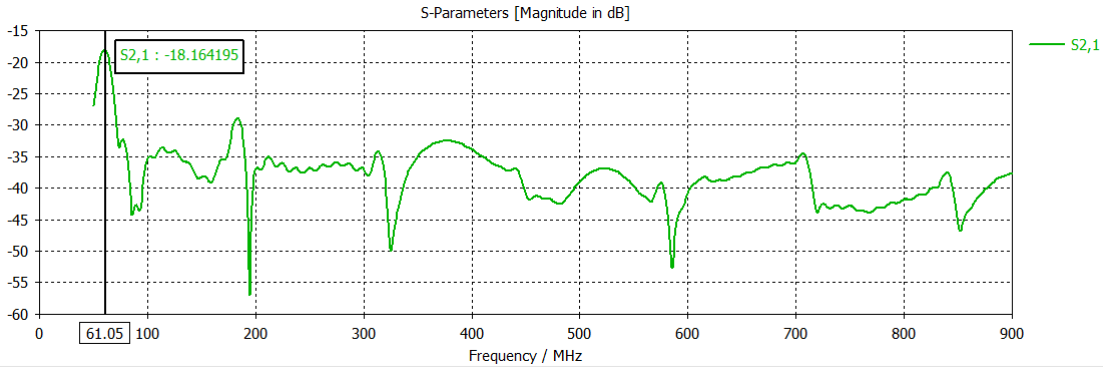

Figure 5.2 S_{21} parameter demonstrating the antenna behavior without any shielding material (The Black marker shows that S21 is -18 dB at 61 MHz).

Simulation results are summarized as in the Table 5.1.

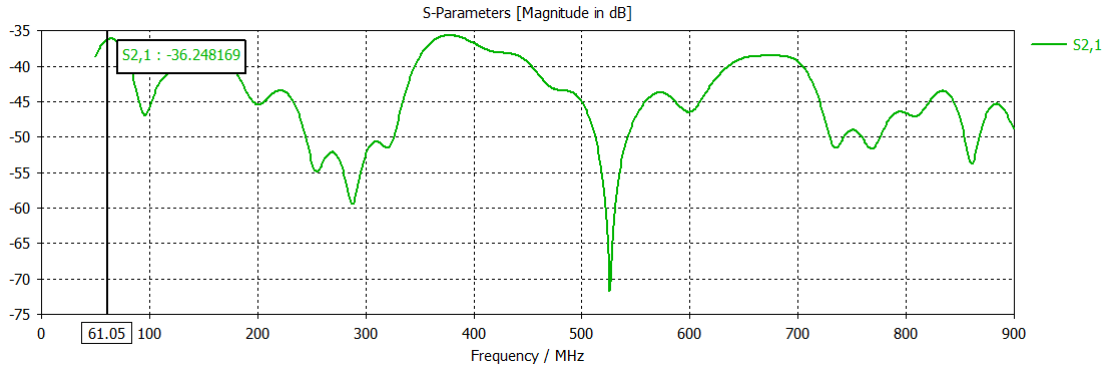

Figure 5.3 S_{21} parameter demonstrating the antenna behavior with plane copper tape shielding material (The Black marker shows that S21 is -36 dB at 61 MHz).

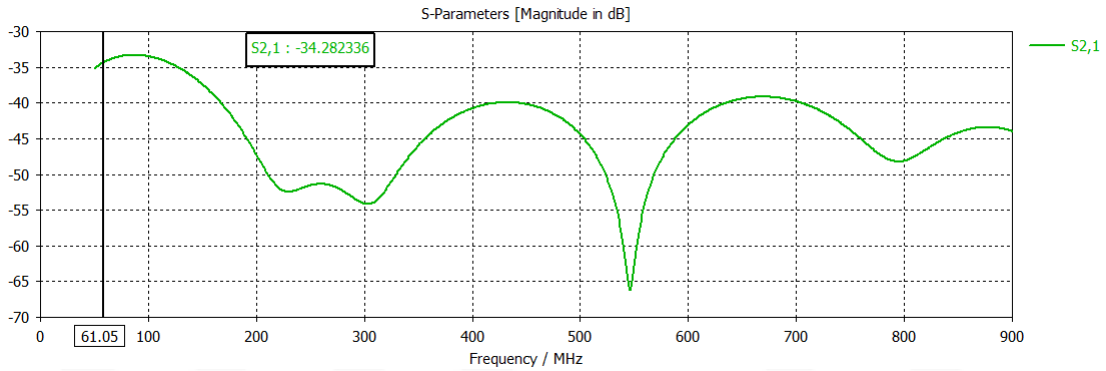

Figure 5.4 S_{21} parameter demonstrating the antenna behavior with plane copper powder-epoxy mixture shielding material (The Black marker shows that S21 is -34 dB at 61 MHz).

5.2 Experiment Results

Experiments were performed in a phantom container as demonstrated in Figure (4.5) and measurements were taken with Rohde and Schwarz ZVB 4 Vector Network Analyzer and recorded S-parameters. First, coaxial cables with a common copper ground plane were inserted in the container and fixed with rubber seal rings in order to ensure impermeability. Then, phantom gel was poured into the container cautiously. In Figure(5.9, 5.10), scattering (S_{11} and S_{21}) parameters of the monopole antennas are presented. Three different shielding materials including a commercial copper tape, copper powder-epoxy mixture and conductive silver base ink were measured quantitatively. S_{21} results of this materials with two different geometrical approaches are represented in Figure(5.11, 5.12, 5.13, 5.14, 5.15 and 5.16).

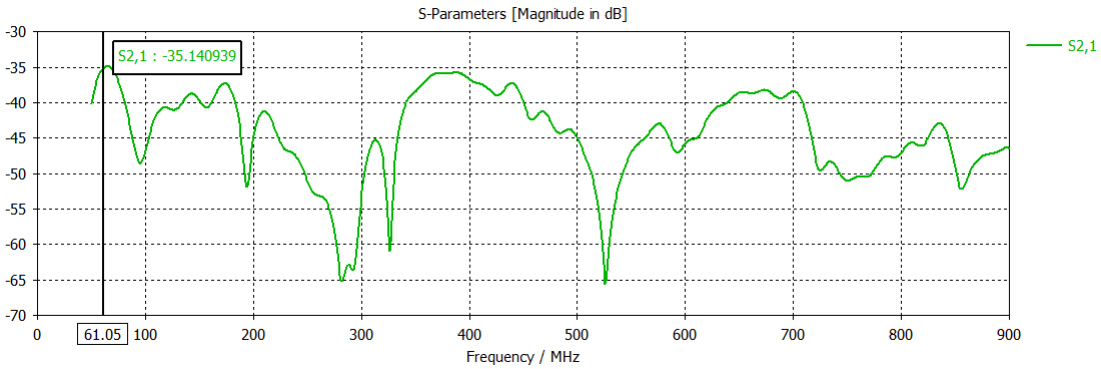

Figure 5.5 S_{21} parameter demonstrating the antenna behavior with plane silver shielding material (The Black marker shows that S21 is -35 dB at 61 MHz).

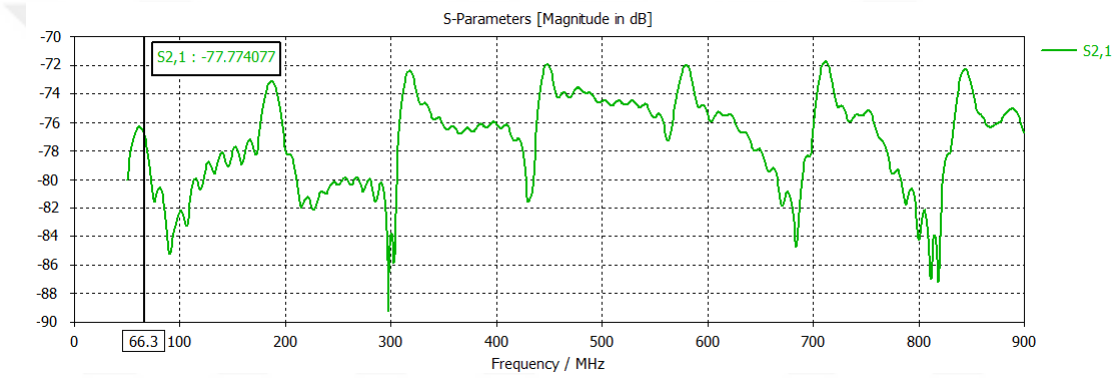

Figure 5.6 S_{21} parameter demonstrating the antenna behavior with cylindrical copper tape shielding material (The Black marker shows that S21 is -77.8 dB at 66 MHz).

Experiment and simulation results are summarized as in the Table 5.2, and Table 5.4.

In the second experiment monopole antennas were constructed with pure copper wires (wire diameter = 1.5 mm). Copper wires were cut into to quarter wavelength lengths and they were inserted to the phantom. The vector network analyzer results are summarized as in the Table 5.3. S_{21} parameter were measured as -26.6 dB when there is no shielding material in between or surrounding any of the monopole antennas.

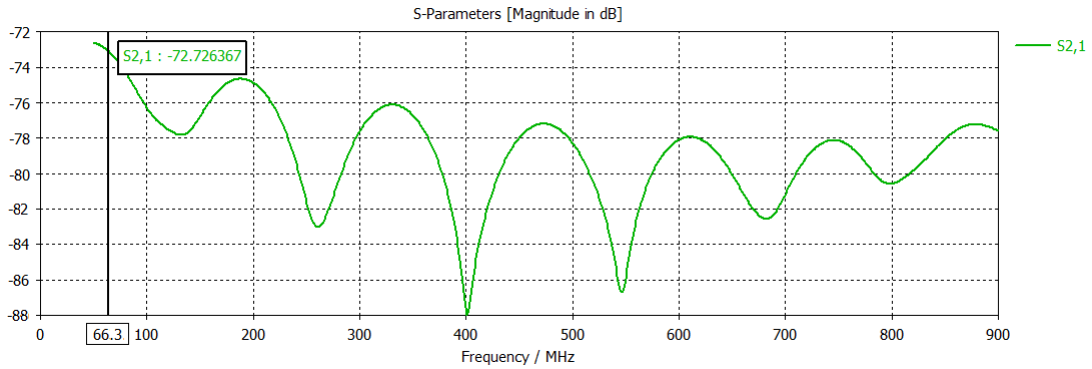

Figure 5.7 S_{21} parameter demonstrating the antenna behavior with cylindrical copper powder-epoxy mixture shielding material (The Black marker shows that S21 is -72.7 dB at 66 MHz).

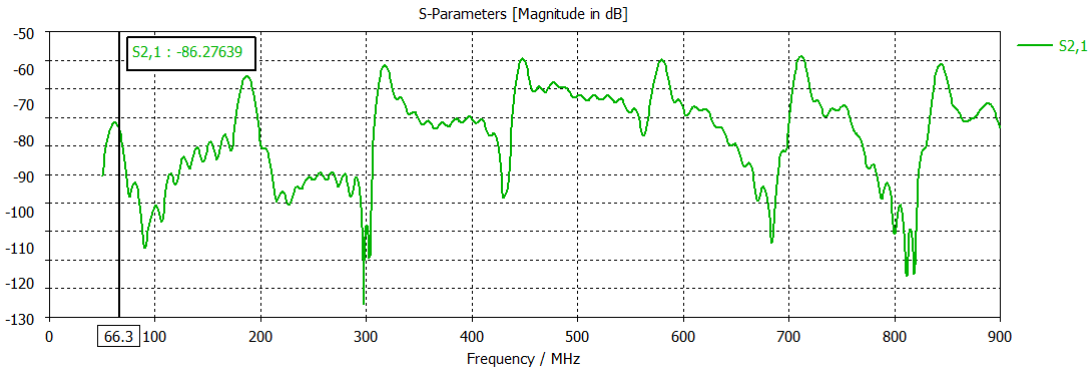

Figure 5.8 S_{21} parameter demonstrating the antenna behavior with cylindrical silver shielding material (The Black marker shows that S21 is -86.3 dB at 66 MHz).

Table 5.1
S_{21} simulation results were summarized for different configurations.

Configuration	S_{21} results in phantom (dB)
Without any shielding material	-18.16
Copper tape plane shield	-36.25
Copper powder-epoxy mixture plane shield	-34.28
Silver ink plane shield	-35.14
Copper tape cylindrical shield	-77.77
Copper powder-epoxy mixture cylindrical shield	-72.72
Silver cylindrical shield	-86.3

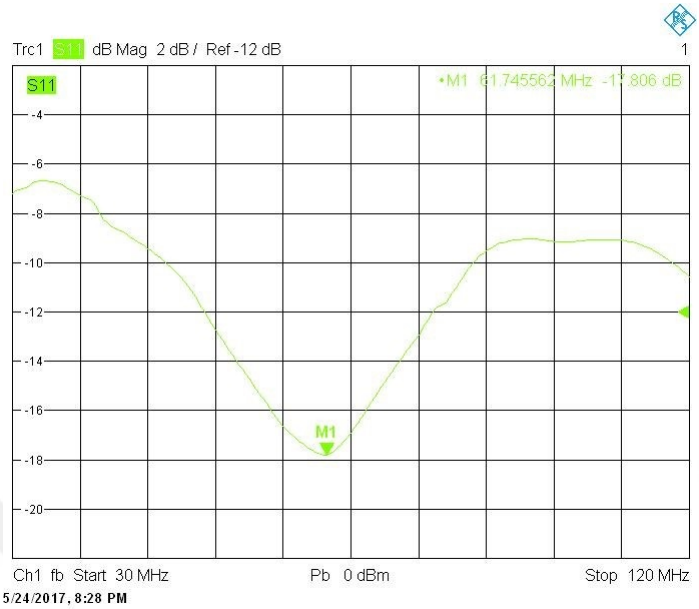

Figure 5.9 S_{11} results of the monopole antennas in the phantom (The Green marker shows that S21 is -17.8 dB at 61 MHz).

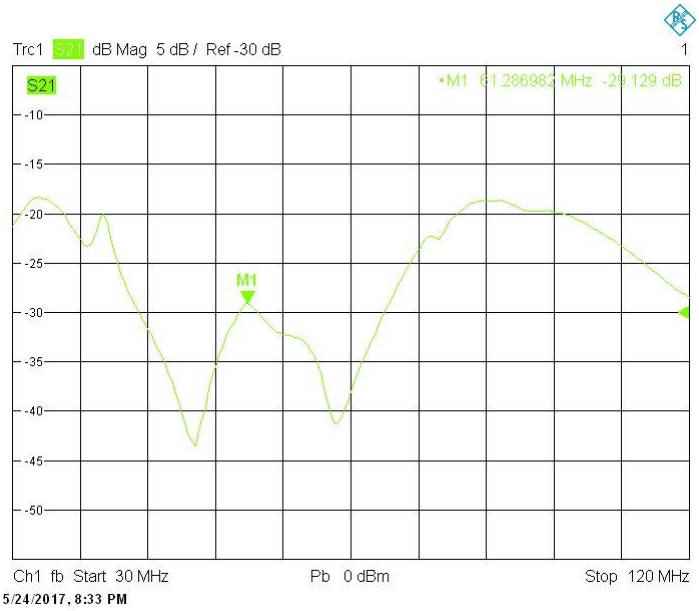

Figure 5.10 S_{21} results of the monopole antennas in the phantom (The Green marker shows that S21 is -29 dB at 61 MHz).

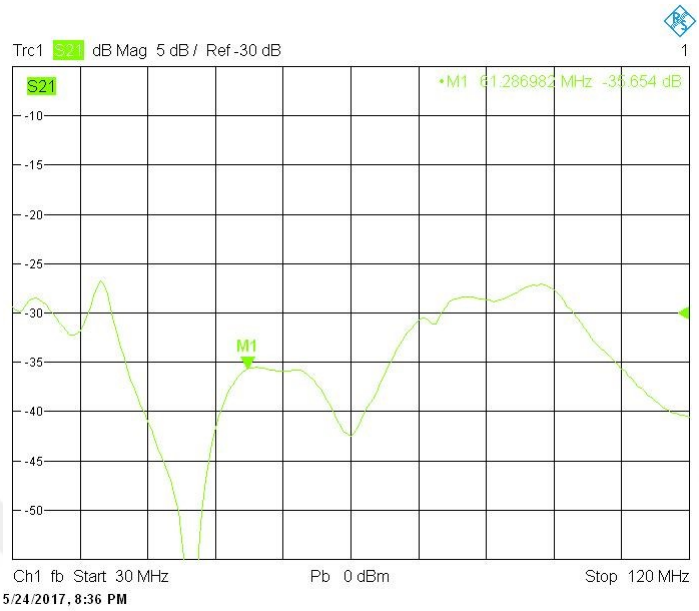

Figure 5.11 S_{21} results of the monopole antennas in the phantom with a commercial copper tape shielding in a planar geometry (The Green marker shows that S21 is -35.7 dB at 61 MHz).

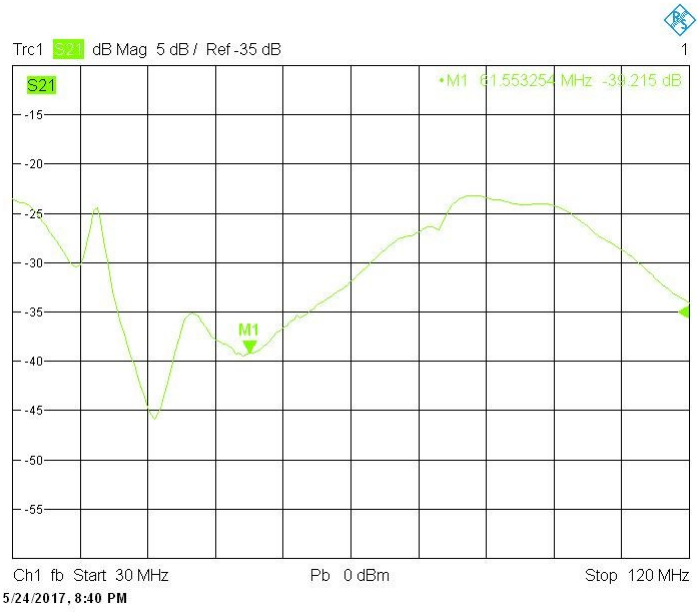

Figure 5.12 S_{21} results of the monopole antennas in the phantom with a copper powder-epoxy mixture shielding planar geometry (The Green marker shows that S21 is -39.2 dB at 61 MHz).

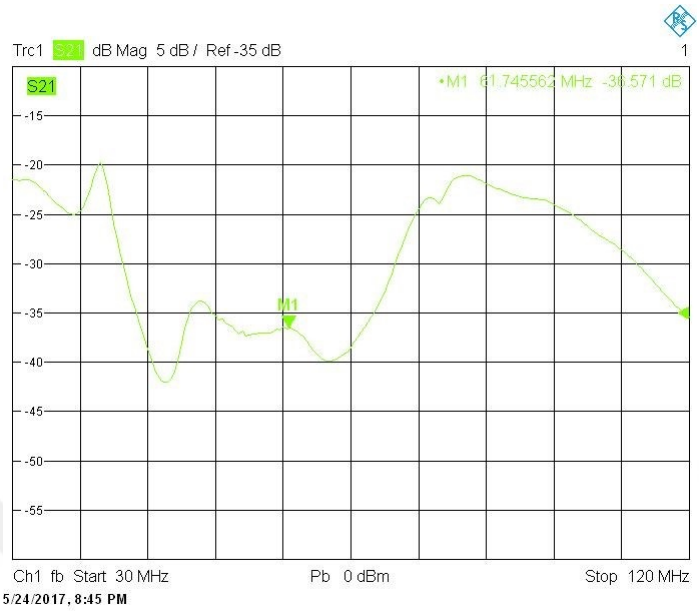

Figure 5.13 S_{21} results of the monopole antennas in the phantom with a conductive silver ink shielding planar geometry (The Green marker shows that S21 is -36.6 dB at 61 MHz).

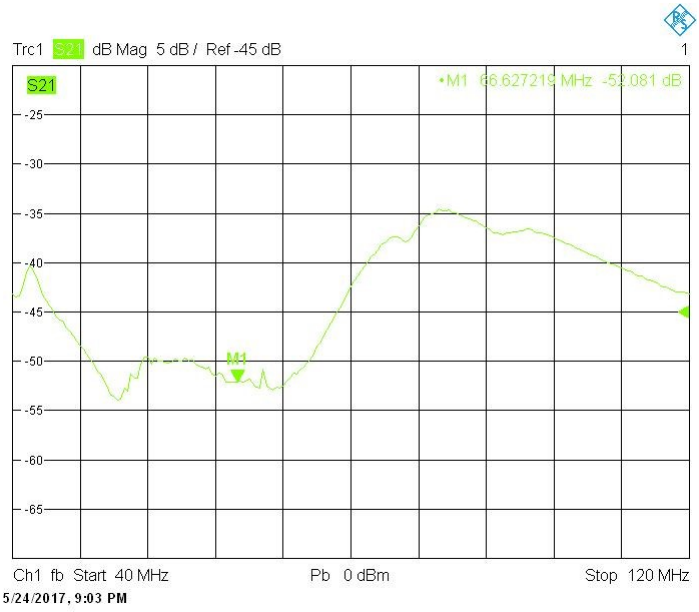

Figure 5.14 S_{21} results of the monopole antennas in the phantom with a commercial copper tape shielding in a cylindrical geometry (The Green marker shows that S21 is -52 dB at 66 MHz).

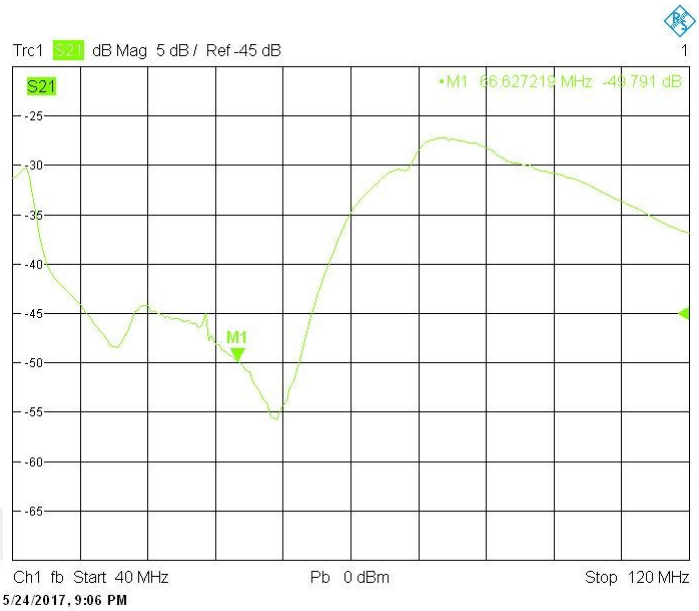

Figure 5.15 S_{21} results of the monopole antennas in the phantom with a copper powder-epoxy mixture shielding in a cylindrical geometry (The Green marker shows that S21 is -49.8 dB at 66 MHz).

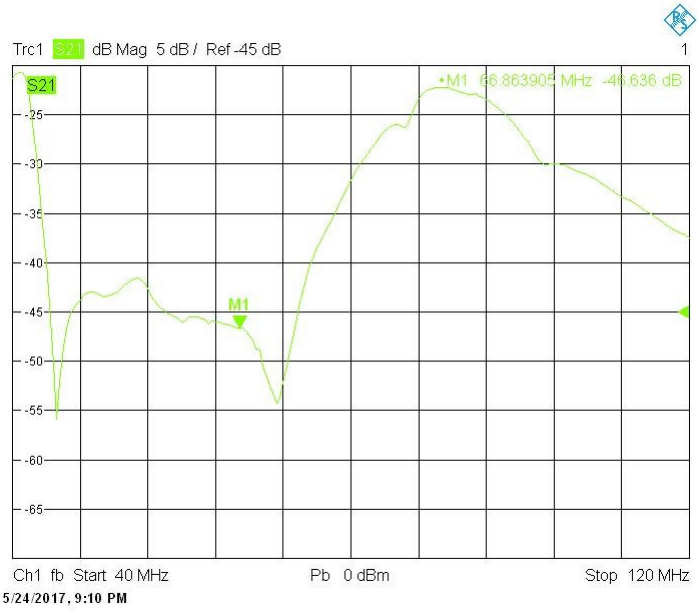

Figure 5.16 S_{21} results of the monopole antennas in the phantom with a conductive silver ink shielding in a cylindrical geometry (The Green marker shows that S21 is -46.6 dB at 66 MHz).

Table 5.2
S_{21} simulation and experimental results were summarized for different measurement configurations.

Configuration	S_{21} results in phantom (dB)	S_{21} simulation results (dB)
Without any shielding material	-29.13	-18.16
Copper tape plane shield	-35.65	-36.24
Copper-epoxy mixture plane shield	-39.22	-34.28
Conductive silver ink plane shield	-36.57	-35.14
Copper tape cylindrical shield	-52.08	-77.77
Copper-epoxy mixture cylindrical shield	-49.79	-72.72
Conductive silver ink cylindrical shield	-46.63	-86.3

Table 5.3
S_{21} results for the second experiment performed with the thick copper wires for different measurement configurations.

Shielding geometry	Copper tape	Copper powder-epoxy	Silver conductive ink
Plane shielding	-40.3	-34.1	-39.1
Cylindrical shielding	-65.7	-51.3	-75.9

Table 5.4
S_{21} simulation and experimental results were summarized for different measurement configurations.

S_{21} results (dB) in phantom for configurations	Experiment-1 (Coaxial cable)	Experiment-2 (Copper wire)	Simulation results
Without any shielding material(61MHz)	-29.13	-26.61	-18.16
Copper tape plane shield(61MHz)	-35.65	-40.3	-36.24
Copper-epoxy plane shield(61MHz)	-39.22	-34.1	-34.28
Conductive silver ink plane shield(61MHz)	-36.57	-39.1	-35.14
Copper tape cylindrical shield(66MHz)	-52.08	-65.7	-77.77
Copper-epoxy cylindrical shield(66MHz)	-49.79	-51.3	-72.72
Conductive silver ink cylindrical shield(66MHz)	-46.63	-75.9	-86.3

6. CONCLUSION

Convenient designs for device tip visualization and tracking during the clinical interventional procedures is a widely studied topic. This study is a part of a novel acousto-optic signal transmission line design for MR compatible interventional devices, which was implemented in collaboration with Prof. Dr. Levent Degertekin and his research group (The George W. Woodruff School of Mechanical Engineering, Georgia Institute of Technology) at the National Heart, Lung and Blood Institute (NHLBI, National Institutes of Health). Acousto-optic active MR marker consists of a coil, a piezoelectric transducer and a Fiber Bragg Grating (FBG) sensor at the distal end of an optical fiber. Thus, with this concept, radio-frequency (RF) related heating concerns due to metallic components under MRI are aimed to be eliminated.

Previous in vitro phantom experiments showed that the acousto-optical transmission line is applicable for RF signal transmission through the optical fiber. However SNR results of the received RF signals also demonstrated that the sensitivity of the overall system needs to be improved. While this improvement can be achieved by optimizing the coil, ultrasound transducer and FBG sensor, interference between the piezoelectric transducer and MR scanner is also another factor reducing the SNR.

Conventionally RF shields are made of bulky metal cages thus a more convenient method is needed. Conductive inks and adhesives are commonly used in electronic devices since they have close conductivity values as the conventional conductive materials. Also they are cost-effective, abundant and flexible solutions for especially small target areas. The requirement of small profile for interventional cardiovascular devices made coating solutions compulsory.

This thesis study covers simulations and phantom experiment for the shielding effectiveness measurements. With this measurement setup, shielding effectiveness of three different materials including a copper tape, a copper powder-epoxy mixture and

a conductive silver ink was measured. Monopole antennas were constructed aiming to measure the scattering parameters and thus shielding effectiveness was evaluated. for construction convenience (also for the convenience of gelled phantom and container construction), quarter wavelength antennas (the overall length is equal to approximately 1.2 meters) were constructed from commercial coaxial cables instead of constructing the antennas at the overall wavelength in air at 1.5T MR frequency (for 63.66 MHz frequency, one wavelength in air equals to approximately 4.8 meters). Also, the use of coaxial cable which has a 50 ohm characteristic impedance value, matches with the vector network analyzer input impedance and therefore increased the antenna efficiency. Regarding the monopole antenna design, copper wires were selected because of their higher conductivity and better performance as an antenna. Although thick copper wires have a better quality factor when compared to the coaxial transmission line, frequency sensitive design is essential for an accurate shielding effectiveness measurement.

Before conducting an experiment, in order to optimize the design to fit the requirements and saving materials and time, it is very important to make the simulations at the beginning. Thus simulations were made in a commercial electromagnetic simulation program $CST^{®}$ (Computer Simulation Technology AG., Dassault Systems). Regarding the configuration of the monopole antennas within the phantom without any shielding material in between or surrounding one of the monopole antennas, simulation results showed a different behavior regarding the scattering parameters(S_{21}). This difference was mainly due to the experiment set-up preparation related imperfections such as inherently imperfect RG-58 coaxial cable, imperfect soldering of the thick copper wire to the SMA connector or the inhomogeneity of the gelled saline (phantom gel). According to the experiments, monopole antenna transmission coefficient (S_{21}), was different then the simulation results being -29.13 dB (monopole antennas made of the coaxial cables), -26.6 dB (monopole antennas made of thick copper wires) and -18.16 dB (simulation result in CST) respectively.

Regarding the planar geometry shielding (for both copper tape, copper-epoxy mixture and conductive silver ink materials), simulation results and experimental results were similar. In fact, simulations demonstrated that for the planar geometry,

there is no significant difference between a copper and a silver shielding. According to the experimental results, first experiment showed that among three different shielding materials copper powder-epoxy blend has a better performance. In the second experiment, conductive silver ink followed closely the copper tape.

On the other hand, cylindrical geometry showed a better performance when compared to the planar geometry. Since the electromagnetic waves are being radiated through all directions, those results were as expected. Differences between the simulation and experiment results were mainly due to the reason that materials like copper and silver were perfectly defined in the material library of the simulation program.

It was demonstrated that the electromagnetic radiation interference can be prevented using MR compatible shielding materials. Since copper has a magnetic permeability close to the human tissue, a discernable image artifact during MRI is not predicted. With the simulation design, it was successfully demonstrated that shielding properties of metals with different thickness values, geometries and dimensions can be predicted before conducting the experiments. The measurement set-up including the monopole antennas, phantom container, different shielding geometries (planar and cylindrical) and their connections were successfully implemented and experiment results were compared to the simulation results. It was also acknowledged that antennas need to be optimized for a specific frequency range. It may be beneficial to improve the antenna in terms of the radiated power and antenna gain.

In the future studies, it is planned to optimize further the shielding geometry. Frequency selective surfaces, with the intention of creating a bandpass filter for the concerned frequency range, will be designed and implemented for different MR compatible shielding materials. Also, for the future evaluations, the new shielding material coated housing design for the piezoelectric transducer of an acousto-optic transmission line will be tested under MRI and the improvement on the SNR of the received signal will be evaluated.

7. APPENDIX

7.1 Appendix A

MATLAB Code for the wavelength calculation:

pi = 3.14;

f = 63.66e6;

$w = 2 * pi * f$;

u = 1;

$u0 = 4 * pi * 1e - 7$;

e = 77;

$e0 = 8.854 * 1e - 12$;

conductivity = 0.47;

$lambda =$

$(2*pi)/(w*sqrt(u*e*u0*e0/2))/(sqrt(1+sqrt(1+(conductivity^2/((w^2)*((e*e0)^2)))))$

$length_{monopole} = lambda/4$

REFERENCES

1. Quick, H. H., M. O. Z. H. Kuehl, G. Kaiser, S. A. S. Massing, S. Bosk, and M. E, "Interventional magnetic resonance angiography with no strings attached: Wireless active catheter visualization," *Magnetic Resonance in Medicine*, Vol. 53, pp. 446–455, Feb 2005.

2. Baysoy, E., D. K. Yildirim, C. Ozsoy, S. Mutlu, and O. Kocaturk, "Thin film based semi-active resonant marker design for low profile interventional cardiovascular mri devices," *MAGMA*, Vol. 30, pp. 93–101, Feb 2017.

3. Saikus, C. E., K. Ratnayaka, I. M. Barbash, J. H. Colyer, O. Kocaturk, A. Z. Faranesh, and R. J. Lederman, "Mri-guided vascular access with an active visualization needle," *Journal of Magnetic Resonance Imaging*, Vol. 34, pp. 1159–1166, Nov 2011.

4. Ladd, M. E., G. G. Zimmermann, H. H. Quick, J. F. Debatin, P. Boesiger, G. K. von Schulthess, and G. C. McKinnon, "Active mr visualization of a vascular guidewire in vivo," *Journal of Magnetic Resonance Imaging*, Vol. 8, pp. 220–225, Jan-Feb 1998.

5. Kocaturk, O., A. H. Kim, C. E. Saikus, M. A. Guttman, A. Z. Faranesh, C. Ozturk, and R. J. Lederman, "Active two-channel 0.035" guidewire for interventional cardiovascular mri," *Journal of Magnetic Resonance Imaging*, Vol. 30, pp. 461–465, Aug 2009.

6. Quick, H. H., H. Kuehl, G. Kaiser, D. Hornscheidt, K. P. Mikolajczyk, S. Aker, J. F. Debatin, and M. E. Ladd, "Interventional mra using actively visualized catheters, truefisp, and real-time image fusion," *Magnetic Resonance in Medicine*, Vol. 49, pp. 129–137, Jan 2003.

7. Wong, E. Y., Q. Zhang, J. L. Duerk, J. S. Lewin, and M. Wendt, "An optical system for wireless detuning of parallel resonant circuits," *Journal of Magnetic Resonance Imaging*, Vol. 12, pp. 632–638, Oct 2000.

8. Bagwell, R. M., J. M. McManaman, and R. C. Wetherhold, "Short shaped copper fibers in an epoxy matrix: Their role in a multifunctional composite," *Composites Science and Technology*, Vol. 66, pp. 522–530, Mar 2006.

9. Morari, C., and I. Balan, "Methods for determining shielding effectiveness of materials," *Journal of Electrotehnica, Electronica, Automatica*, Vol. 63, pp. –, 2015.

10. Raval, A. N., J. D. Telep, M. A. Guttman, C. Ozturk, M. Jones, R. B. Thompson, V. J. Wright, W. H. Schenke, R. DeSilva, R. J. Aviles, V. K. Raman, M. C. Slack, and R. J. Lederman, "Real-time magnetic resonance imaging-guided stenting of aortic coarctation with commercially available catheter devices in swine.," *Circulation*, Vol. 112, pp. 699–706, Aug 2005.

11. Kleinerman, R. A., "Cancer risks following diagnostic and therapeutic radiation exposure in children," *Pediatric Radiology*, Vol. 36, pp. 121–125, Sep 2006.

12. Elgort, D. R., C. M. Hillenbrand, and S. Zhang, "Image-guided and -monitored renal artery stenting using only mri," *Journal of Magnetic Resonance Imaging*, Vol. 23, pp. 619–627, 2006.

13. Raman, V. K., P. V. Karmarkar, M. A. Guttman, A. J. Dick, D. C. Peters, C. Ozturk, B. S. Pessanha, R. B. Thompson, A. N. Raval, R. DeSilva, R. J. Aviles, E. Atalar, E. R. McVeigh, and R. J. Lederman, "Real-time magnetic resonance-guided endovascular repair

of experimental abdominal aortic aneurysm in swine.," *Journal of the American College of Radiology*, Vol. 45, pp. 2069–2077, 2005.

14. Buecker, A., E. Spuentrup, and R. Grabitz, "Magnetic resonance-guided placement of atrial septal closure device in animal model of patent foramen ovale.," *Circulation*, Vol. 106, pp. 511–515, 2002.

15. Kuehne, T., S. Yilmaz, and C. Meinus, "Magnetic resonance imaging-guided transcatheter implantation of a prosthetic valve in aortic valve position: feasibility study in swine.," *Journal of the American College of Radiology*, Vol. 44, pp. 2247–2249, 2004.

16. Susil, R. C., C. J. Yeung, H. R. Halperin, A. C. Lardo, and E. Atalar, "Multifunctional interventional devices for mri: a combined electrophysiology/mri catheter.," *Magnetic Resonance in Medicine*, Vol. 47, pp. 594–600, 2002.

17. Dukkipati, S. R., R. Mallozi, and E. J. Schmidt, "Electroanatomic mapping of the left ventricle in a porcine model of chronic myocardial infarction with magnetic resonance-based catheter tracking.," *Circulation*, Vol. 118, pp. 853–862, 2008.

18. Krueger, S., O. Lips, and B. David, "Towards mr-guided ep interventions using an rf-safe approach.," *Journal of Cardiovascular Magnetic Resonce Imaging*, Vol. 11, no. (Suppl), pp. O84–, 2009.

19. Lotz, J., "Interventional vascular mri: moving forward," *European Heart Journal*, Vol. 34, pp. 327–329, Nov 2013.

20. Raman, V. K., and R. J. Lederman, "Interventional cardiovascular magnetic resonance imaging," *Trends in Cardiovascular Medicine*, Vol. 17, pp. 196–202, Aug 2007.

21. Shellock, F. G., T. O. Woods, and J. V. 3rd Crues, "Mr labeling information for implants and devices: explanation of terminology.," *Radiology*, Vol. 253, pp. 26–30, Oct 2009.

22. Tsai, L. L., A. K. Grant, K. J. Mortele, J. W. Kung, and M. P. Smith, "A practical guide to mr imaging safety: What radiologists need to know.," *RadioGraphics*, Vol. 35, pp. 1722–1737, Oct 2015.

23. Nitz, W. R., A. O, W. R, C. M, M. L, and J. Link, "On the heating of linear conductive structures as guide wires and catheters in interventional mri," *Journal of Magnetic Resonance Imaging*, Vol. 13, pp. 105–114, Jan 2001.

24. Bushberg, J. T., J. A. Seibert, E. M. L. Jr., and J. M. Boone, *The Essential Physics of Medical Imaging*, Philadelphia: LIPPINCOTT WILLIAMS AND WILKINS, 2011.

25. on Radiation Protection, N. C., and Measurements, "Medical radiation exposure of the u.s. population greatly increased since the early 1980s," pp. –, Mar.

26. Rogers, T., K. Ratnayaka, and R. J. Lederman, "Mri catheterization in cardiopulmonary disease," *Chest*, Vol. 145, pp. 30–36, Jan 2014.

27. Ratnayaka, K., A. Z. Faranesh, M. S. Hansen, A. M. Stine, M. Halabi, I. M. Barbash, W. H. Schenke, V. J. Wright, L. P. Grant, P. Kellman, O. Kocaturk, and R. J. Lederman, "Real-time mri-guided right heart catheterization in adults using passive catheters," *European heart journal*, Vol. 34, pp. 380–389, Feb 2012.

28. Dick, A. J., V. K. Raman, A. N. Raval, M. A. Guttman, R. B. Thompson, C. Ozturk, D. C. Peters, A. M. Stine, V. J. Wright, W. H. Schenke, and R. J. Lederman, "Invasive human magnetic resonance imaging: feasibility during revascularization in a combined xmr suite," *Catheterization and cardiovascular interventions*, Vol. 64, pp. 265–274, Mar 2005.

29. Lederman, R. J., "Cardiovascular interventional magnetic resonance imaging," *Circulation*, Vol. 112, pp. 3009–3017, Nov 2005.

30. on Non-Ionizing Radiation Protection, I. C., "Icnirp statement on the guidelines for limiting exposure to time-varying electric, magnetic, and electromagnetic fields (up to 300 ghz).," *Health Physics*, Vol. 97, no. 3, pp. 257–258, 2009.

31. Shellock, F. G., "Radiofrequency energy-induced heating during mr procedures: A review," *Journal of Magnetic Resonance Imaging*, Vol. 12, pp. 30–36, Jul 2000.

32. Yeung, C. J., R. C. Susil, and E. Atalar, "Rf safety of wires in interventional mri: Using a safety index," *Magnetic Resonance in Medicine*, Vol. 47, pp. 187–193, Jan 2002.

33. Settecase, F., S. W. Hetts, A. J. Martin, T. P. L. Roberts, A. F. Bernhardt, L. Evans, V. Malba, M. Saeed, R. L. Arenson, W. Kucharzyk, and M. W. Wilson, "Rf heating of mri-assisted catheter steering coils for interventional mri," *Academic Radiology*, Vol. 18, pp. 277–285, Mar 2011.

34. Bell, J. A., C. E. Saikus, K. Ratnayaka, V. Wu, M. Sonmez, A. Z. Faranesh, J. H. Colyer, R. J. Lederman, and O. Kocaturk, "A deflectable guiding catheter for real-time mri guided interventions.," *Journal of Magnetic Resonance Imaging*, Vol. 35, pp. 908–915, Apr 2012.

35. Armenean, C., E. Perrin, M. Armenean, O. Beuf, F. Pilleul, and H. Saint-Jalmes, "Rf-induced temperature elevation along metallic wires in clinical magnetic resonance imaging: Influence of diameter and length," *Magnetic Resonance in Medicine*, Vol. 52, pp. 1200–1206, Nov 2004.

36. Yeung, C. J., R. C. Susil, and E. Atalar, "Rf heating due to conductive wires during mri depends on the phase distribution of the transmit field.," *Magnetic Resonance in Medicine*, Vol. 48, pp. 1096–1098, Dec 2002.

37. Yeung, C. J., P. Karmarkar, and E. R. McVeigh, "Minimizing rf heating of conducting wires in mri.," *Magnetic Resonance in Medicine*, Vol. 58, pp. 1028–1034, Nov 2007.

38. Wang, W., "Magnetic resonance–guided active catheter tracking," *Magnetic Resonance Imaging Clinics in North America*, Vol. 23, pp. 579–589, Nov 2015.

39. Ladd, M. E., and H. H. Quick, "Reduction of resonant rf heating in intravascular catheters using coaxial chokes.," *Magnetic Resonance in Medicine*, Vol. 43, pp. 615–619, Apr 2000.

40. Weiss, S., P. Vernickel, T. Schaeffter, V. Schulz, and B. Gleich, "Transmission line for improved rf safety of interventional devices.," *Magnetic Resonance in Medicine*, Vol. 54, pp. 182–189, Jul 2005.

41. Saikus, C. E., K. Ratnayaka, I. M. Barbash, J. H. Colyer, O. Kocaturk, A. Z. Faranesh, and R. J. Lederman, "Mri-guided vascular access with an active visualization needle," *Journal of Magnetic Resonance Imaging*, Vol. 34, pp. 1159–1166, Nov 2011.

42. Eryaman, Y., B. Akin, and E. Atalar, "Reduction of implant rf heating through modification of transmit coil electric field," *Magnetic Resonance in Medicine*, Vol. 65, pp. 1305–1313, May 2011.

43. Liu, C. Y., K. Farahani, D. S. K. Lu, G. Duckwiler, and A. Oppelt, "Safety of mri-guided endovascular guidewire applications," *Journal of Magnetic Resonance Imaging*, Vol. 12, pp. 75–78, Jul 2000.

44. Bottomley, P. A., "Turning up the heat on mri," *Journal of the American College of Radiology*, Vol. 5, pp. 853–855, Jul 2008.

45. Wong, E. Y., Q. Zhang, J. L. Duerk, J. S. Lewin, and M. Wendt, "An optical system for wireless detuning of parallel resonant circuits," *Journal of Magnetic Resonance Imaging*, Vol. 12, pp. 632–638, Oct 2000.

46. Bakker, C. J., R. M. Hoogeveen, J. Weber, J. J. van, M. A. Viergever, and W. P. M. Vaals, "Visualization of dedicated catheters using fast scanning techniques with potential for mr-guided vascular interventions," *Magnetic Resonance in Medicine*, Vol. 36, pp. 816–820, Dec 1996.

47. Rubin, D. L., A. V. Ratner, and S. W. Young, "Magnetic susceptibility effects and their application in the development of new ferromagnetic catheters for magnetic resonance imaging," *Investigative Radiology*, Vol. 25, pp. 1325–1332, Dec 1990.

48. Sillerud, L. O., A. F. McDowell, N. L. Adolphi, R. E. Serda, D. P. Adams, M. J. Vasile, and T. M. Alam, "1h nmr detection of superparamagnetic nanoparticles at 1 t using a microcoil and novel tuning circuit," *Magnetic Resonance*, Vol. 181, pp. 181–190, Aug 2006.

49. Dharmakumar, R., I. Koktzoglou, R. Tang, K. R. Harris, N. Beohar, and D. Li, "Off-resonance positive contrast imaging of a passive endomyocardial catheter in swine," *Phys. Med. Biol.*, Vol. 53, pp. N249–N257, Jul 2008.

50. Patil, S., O. Bieri, P. Jhooti, and K. Scheffler, "Automatic slice positioning (asp) for passive real-time tracking of interventional devices using projection-reconstruction imaging with echo-dephasing (pride)," *Magnetic Resonance in Medicine*, Vol. 62, pp. 935–942, Oct 2009.

51. Edelman, R. R., P. Storey, E. Dunkle, W. Li, A. Carrillo, A. Vu, and T. J. Carroll, "Gadolinium-enhanced off-resonance contrast angiography," *Magnetic Resonance in Medicine*, Vol. 57, pp. 475–484, Mar 2007.

52. Mekle, R., E. Hofmann, K. Scheffler, and D. Bilecen, "A polymer-based mr-compatible guidewire: A study to explore new prospects for interventional peripheral magnetic resonance angiography(ipmra)," *Journal of Magnetic Resonance Imaging*, Vol. 23, pp. 145–155, Dec 2006.

53. Kozerke, S., S. Hegde, T. Schaeffter, R. Lamerichs, R. Razavi, and D. L. Hill, "Catheter tracking and visualization using 19f nuclear magnetic resonance," *Magnetic Resonance in Medicine*, Vol. 52, pp. 693–697, Sep 2004.

54. Miquel, M. E., S. Hegde, V. Muthurangu, B. J. Corcoran, S. F. Keevil, D. L. G. Hill, and R. S. Razavi, "Visualization and tracking of an inflatable balloon catheter using ssfp in a flow phantom and in the heart and great vessels of patients," *Magnetic Resonance in Medicine*, Vol. 51, pp. 988–995, May 2004.

55. Glowinski, A., G. Adam, A. Bucker, J. Neuerburg, J. J. van Vaals, and R. W. Gunther, "Catheter visualization using locally induced, actively controlled field inhomogeneities," *Magnetic Resonance in Medicine*, Vol. 38, pp. 253–258, Aug 1997.

56. Kuehne, T., R. Fahrig, and K. Butts, "Pair of resonant fiducial markers for localization of endovascular catheters at all catheter orientations," *Journal of Magnetic Resonance Imaging*, Vol. 17, pp. 620–624, May 2003.

57. Adam, G., A. Glowinski, J. Neuerburg, A. B. J. J. van Vaals, and R. W. Gunthe, "Visualization of mr-compatible catheters by electrically induced local field inhomogeneities: Evaluation in vivo," *Journal of Magnetic Resonance Imaging*, Vol. 8, pp. 209–213, Jan-Feb 1998.

58. Quick, H. H., H. Kuehl, G. Kaiser, S. Bosk, J. F. Debatin, and M. E. Ladd, "Inductively coupled stent antennas in mri," *Magnetic Resonance in Medicine*, Vol. 48, pp. 781–790, Nov 2002.

59. Wong, E. Y., Q. Zhang, J. L. Duerk, J. S. Lewin, and M. Wendt, "An optical system for wireless detuning of parallel resonant circuits," *Magnetic Resonance in Medicine*, Vol. 12, pp. 632–638, Oct 2000.

60. Celik, H., A. Uluturk, T. Tali, and E. Atalar, "A catheter tracking method using reverse polarization for mr-guided interventions," *Magnetic Resonance in Medicine*, Vol. 58, pp. 1224–1231, Dec 2007.

61. Wang, W., "Magnetic resonance-guided active catheter tracking," *Magnetic Resonance Imaging Clinics*, Vol. 23, pp. 579–589, Nov 2015.

62. Ackerman, J., M. Offutt, and R. U. Buxton, "Rapid 3d tracking of small rf coils," in *Proceedings of the 5th annual meeting of SMRM*, (Montreal–Canada), SMRM for Society for Magnetic Resonance in Medicine, 19-22 Aug 1986.

63. Dumoulin, C. L., S. P. Souza, and R. D. Darrow, "Real-time position monitoring of invasive devices using magnetic resonance," *Magnetic Resonance in Medicine*, Vol. 29, pp. 411–415, Mar 1993.

64. Ladd, M. E., P. Erhart, J. F. Debatin, E. Hofmann, P. Boesiger, G. K. von Schulthess, and G. C. McKinnon, "Guidewire antennas for mr fluoroscopy," *Magnetic Resonance in Medicine*, Vol. 37, pp. 891–897, June 1997.

65. Burl, M., G. A. Coutts, D. J. Herlihy, R. Hill-Cottingham, J. F. Eastham, J. V. Hajnal, and I. R. Young, "Twisted-pair rf coil suitable for locating the track of a catheter," *Magnetic Resonance in Medicine*, Vol. 41, pp. 636–638, Mar 1999.

66. Leung, D. A., J. F. Debatin, S. Wildermuth, G. C. McKinnon, D. Holtz, C. L. Dumoulin, R. D. Darrow, E. Hofmann, and G. K. von Schulthess, "Intravascular mr tracking catheter: preliminary experimental evaluation," *American Journal of Roentgenology*, Vol. 164, pp. 1265–1270, May 1995.

67. McKinnon, G. C., J. F. Debatin, D. A. Leung, S. Wildermuth, D. J. Holtz, and G. K. von Schulthess, "Towards active guidewire visualization in interventional magnetic resonance imaging," *MAGMA*, Vol. 4, pp. 13–8, Mar 1996.

68. Atalar, E., P. A. Bottomley, and E. A. Zerhouni, "A flexible catheter coil for imaging and spectroscopy of atherosclerotic plaques," in *Proceedings of the SMR 3rd Annual Meeting*, (Nice–France), pp. –, SMR for Society for Magnetic Resonance, 1-4 Sept 1995.

69. Ocali, O., and E. Atalar, "Intravascular magnetic resonance imaging using a loopless catheter antenna," *Magnetic Resonance in Medicine*, Vol. 37, pp. 112–118, Jan 1997.

70. Serfaty, J. M., X. Yang, P. Aksit, H. H. Quick, M. Solaiyappan, and E. Atalar, "Toward mri-guided coronary catheterization: visualization of guiding catheters, guidewires, and anatomy in real time," *Journal of Magnetic Resonance Imaging*, Vol. 12, pp. 590–594, Oct 2000.

71. Konings, M. K., L. W. Bartels, C. F. P. van Swol, and C. J. G. Bakker, "Development of an mr-safe tracking catheter with a laser-driven tip coil," *Journal of Magnetic Resonance Imaging*, Vol. 13, pp. 131–135, Jan 2001.

72. Fandrey, S., S. Weiss, and J. Muller, "Development of an active intravascular mr device with an optical transmission system," *IEEE Transactions On Medical Imaging*, Vol. 27, pp. –, Dec 2008.

73. Fandrey, S., S. Weiss, and J. Muller, "A novel active mr probe using a miniaturized optical link for a 1.5-t mri scanner," *Magnetic Resonance in Medicine*, Vol. 67, pp. 148–155, Aug 2012.

74. Bock, M., R. Umathum, J. Sikora, S. Brenner, E. N. Aguor, and W. Semmler, "A faraday effect position sensor for interventional magnetic resonance imaging," *Physics in Medicine and Biology*, Vol. 51, pp. 999–1009, Mar 2006.

75. Reiss, S., A. Bitzer, and M. Bock, "An optical setup for electric field measurements in mri with high spatial resolution," *Physics in Medicine and Biology*, Vol. 60, pp. 4355–4370, Jun 2015.

76. Webb, A. G., "Radiofrequency microcoils in magnetic resonance," *Progress in Nuclear Magnetic Resonance Spectroscopy*, Vol. 31, pp. 1–42, July 1997.

77. Qian, C., G. Zabow, and A. Koretsky, "Engineering novel detectors and sensors for mri," *Journal of Magnetic Resonance*, Vol. 229, pp. 67–74, July 2013.

78. Massin, C., G. Boero, F. Vincent, J. Abenhaim, P. A. Besse, and R. S. Popovic, "High-q factor rf planar microcoils for micro-scale nmr spectroscopy," *Sensors and Actuators A Physical*, Vol. 97, pp. 280–288, Apr 2002.

79. Wojtczyk, H., H. Graf, P. Martirosian, V. Ballweg, M. Kraiger, J. Pintaske, and F. Schick, "Quantification of direct current in electrically active implants using mri methods," *Zeitschrift für Medizinische Physik*, Vol. 21, pp. 135–146, May 2011.

80. Wild, G., and S. Hinckley, "Acousto-ultrasonic optical fiber sensors: Overview and state-of-the-art," *IEEE Sensors Journal*, Vol. 8, pp. 135–146, July 2008.

81. Betz, D. C., G. Thursby, B. Culshaw, and W. J. Staszewski, "Acousto-ultrasonic sensing using fiber bragg gratings," *Smart Materials and Structures*, Vol. 112, pp. 122–128, Jan 2003.

82. Gururaja, T. R., W. A. Schulze, L. E. Cross, R. E. Newnham, B. A. Auld, and Y. J. Wang, "Piezoelectric composite materials for ultrasonic transducer applications.part i: Resonant modes of vibration of pzt rod-polymer composites," *IEEE Transactions on Sonics and Ultrasonics*, Vol. Su-32, pp. –, July 1985.

83. Hunt, J. W., M. Arditi, and F. S. Foster, "Ultrasound transducers for pulse-echo medical imaging," *IEEE Transactions on Biomedical Engineering*, Vol. BME-30, pp. –, Aug 1983.

84. Cheng, C. H., K. L. Cheng, and W. F. Liu, "Reactive current sensor based on fiber bragg grating and a piezo-electric transducer," *Symposium on Photonics and Optoelectronics (SOPO)*, pp. –, Aug 2012.

85. Wen, H., E. Bennett, and D. G. Wiesler, "Shielding of piezoelectric ultrasonic probes in hall effect imaging," *Ultrason Imaging*, Vol. 20, pp. 206–220, July 1998.

86. Gerold, B., S. Reynolds, A. Melzer, and S. Cochran, "Early exploration of mri-compatible diagnostic ultrasound transducers," in *IEEE International Ultrasonics Symposium Proceedings*, (San Diego–California), IEEE International Ultrasonics Symposium (IUS), 11-14 Oct 2010.

87. Elimat, Z. M., A. M. Zihlif, and G. Ragosta, "Study of ac electrical properties of aluminium–epoxy composites," *Journal of Physics D: Applied Physics*, Vol. 41, pp. 5408–, Jul 2008.

88. "(astm 4935 – 10)standard test method for measuring the electromagnetic shielding effectiveness of planar materials," tech. rep., American Society for Testing and Materials International, Pennsylvania, United States, May 2010.

89. Weiner, M. M., *Monopole Antennas*, New York: CRC, 2003. Available: http:/www.dekker.com.

90. Johnson, R. C., ed., *Antenna Engineering Handbook*, New York: McGraw-Hill Professional, 1992.

91. Ulaby, F. T., *Fundamentals of Applied Electromagnetics*, Upper Saddle River,New Jersey: Prentice-Hall, 1999. p. 279.

92. Kocaturk, O., "Active mri compatible and visible imri catheter," *US patent application*, pp. –, 2010.

93. Y Baziard, S Breton, S. T., and A. Gourdenne, "Dielectric properties of copper powder-epoxy resin composites," *European Polymer Journal*, Vol. 24, pp. 633–638, Dec 1988.

94. Pozar, D. M., *Microwave and RF Design of Wireless Systems*, New York: John Wiley and Sons, Inc., 2001.

95. Hirmizi, N. H. M., M. A. Bakar, W. L. Tan, N. H. H. A. Bakar, J. Ismail, and C. H. See, "Electrical and thermal behavior of copper-epoxy nanocomposites prepared via aqueous to organic phase transfer technique," *Journal of Nanomaterials*, pp. –, Dec 2012.

96. Maurer, C., "(astm f2182 – 09)standard test method for measurement of radio frequency induced heating on or near passive implants during magnetic resonance imaging," tech. rep., American Society for Testing and Materials International, Pennsylvania, United States, 2002.

97. Yaras, Y. S., S. Satir, C. Ozsoy, R. Ramasawmy, A. E. C. Washburn, A. Faranesh, R. Lederman, O. Kocaturk, and L. Degertekin, "Acousto-optic based active mri marker for interventional mri devices," in *25th Annual Meeting and Exhibition International Society for Magnetic Resonance Imaging in Medicine*, (Honolulu–USA), ISMRM International Society for Magnetic Resonance Imaging in Medicine, 22-27 Apr 2017.